Applied Surface Science 755 (2027) 168817

Contents lists available at ScienceDirect

Applied Surface Science

journal homepage: www.elsevier.com/locate/apsusc

Full Length Article

Interface-engineered graphene oxide for controlled nanoparticle organisation and tunable plasmonic response

Patrick Irigo [a], Miriam Roldán-Matilla [b], María Fuencisla Gilsanz [c], Javier Perez-Pineiro [c], Arisbel Cerpa-Naranjo [b,*], Ian Johnston [a], Isabel Lado-Touriño [b,*], Guogang Ren [a,**]

[a] School of Physics, Engineering and Computer Science, University of Hertfordshire, Hatfield AL10 9AB, Herts, UK
[b] Universidad Europea de Madrid. Escuela de Arquitectura, Ingeniería, Ciencia y Computación —STEAM, Departamento de Ingeniería. Campus de Villaviciosa, Calle Tajo s/n, 28670 Villaviciosa de Odón, Madrid, Spain
[c] Universidad Europea de Madrid. Escuela de Arquitectura, Ingeniería, Ciencia y Computación —STEAM, Departamento de Ciencia y Aeroespacial. Campus de Villaviciosa, Calle Tajo s/n, 28670 Villaviciosa de Odón, Madrid, Spain

ARTICLE INFO

Keywords:
Graphene oxide
PEGfunctionalisation
Nanoparticleorganisation
Molecular dynamics
Finite-difference time-domain modelling
Plasmonic response

ABSTRACT

Graphene oxide (GO) surface chemistry influences nanoparticle organisation and optical response, yet these relationships remain poorly integrated across experimental and computational length scales. Here, two GO materials with contrasting surface oxygen contents, GO_{10} and GO_{30}, were examined before and after PEG–NH_2 treatment and incorporation of Ag- and Cu-containing particles using spectroscopy, microscopy, thermal analysis, molecular dynamics (MD) and finite-difference time-domain (FDTD) modelling. Higher surface oxygen content and PEG–NH_2 treatment were associated with greater apparent PEG-associated loading, smaller particle populations and reduced nanoparticle aggregation and apparent contact, with Cu D_{50} decreasing from 22.5 to 7.8 nm. MD simulations showed more favourable interfacial interactions following PEG modification, with contact-area-normalised interaction-energy descriptors supporting stronger interactions at the modified interface. FDTD simulations revealed strong size- and separation-dependent responses, including LSPR redshifts of 96.25 nm for Ag and 61.25 nm for Cu across 10–100 nm. Experiment-informed assemblies exhibited higher resonance quality but weaker extreme hotspots as close particle contacts were reduced across the model series, indicating a trade-off between junction-driven enhancement and a less hotspot-dominated, more spectrally defined response. Overall, the results establish a multiscale structure–property framework linking GO interface chemistry, nanoparticle organisation and predicted electromagnetic response.

1. Introduction

Graphene oxide (GO) provides a chemically tuneable platform for nanomaterial assembly because its oxygen-containing functionalities influence surface reactivity, interfacial interactions and electronic properties [1,2]. Variation in surface oxygen content therefore provides a means of modifying the local environment experienced by supported nanoparticles. Further modification with amine-terminated polyethylene glycol (PEG–NH_2) can alter GO interfacial chemistry and nanoparticle interactions, as demonstrated in PEG-modified graphene systems [3–5]. However, the relationship between GO oxidation level, PEG-associated surface modification and the resulting nanoparticle organisation remains insufficiently quantified across comparable material systems.

These interfacial effects are particularly important for graphene-supported plasmonic nanostructures. The optical response of metal nanoparticles depends on particle size, shape, composition, dielectric environment and interparticle separation [6–8]. Closely spaced particles can undergo plasmon hybridisation, producing resonance shifts and strongly localised electromagnetic fields, with coupling strength decreasing markedly as particle separation increases [9,10]. Far-field quantities such as extinction, absorption and scattering describe

* Corresponding authors.
** Corresponding author.
E-mail addresses: p.irigo2@herts.ac.uk (P. Irigo), miriam.roldan@universidadeuropea.es (M. Roldán-Matilla), mariafuencisla.gilsanz@universidadeuropea.es (M.F. Gilsanz), javier.perez4@universidadeuropea.es (J. Perez-Pineiro), arisbel.cerpa@universidadeuropea.es (A. Cerpa-Naranjo), i.d.johnston@herts.ac.uk (I. Johnston), misabel.lado@universidadeuropea.es (I. Lado-Touriño), g.g.ren@herts.ac.uk (G. Ren).

https://doi.org/10.1016/j.apsusc.2026.168817
Received 9 July 2026; Received in revised form 2 October 2026; Accepted 27 October 2026
Available online 28 October 2026
0169-4332/© 2026 The Authors. Published by Elsevier B.V. This is an open access article under the CC BY license (http://creativecommons.org/licenses/by/4.0/).

complementary aspects of the overall optical response, whereas local $|E/E_0|$ characterises near-field amplification. Although both originate from plasmonic excitation, their magnitudes are not directly proportional because they depend differently on particle geometry, damping and electromagnetic coupling [6,9,10]. GO-supported Ag nanostructures have demonstrated surface-chemistry-dependent plasmonic behaviour [11], while the optical response of Cu nanoparticles is additionally sensitive to oxidation and associated plasmon damping [12,13]. Control of particle size and spatial organisation is therefore important for reproducible optical and SERS-related behaviour [14–16].

Although the influence of graphene surface chemistry on Raman and plasmonic behaviour has been investigated previously, its integration with nanoparticle organisation and multiscale modelling remains limited. Controlled reduction of GO has previously been shown to modify graphene-mediated Raman enhancement through changes in oxygen-containing surface groups [17], while nanoparticle morphology can substantially influence hotspot formation and SERS response [7,8]. At the atomistic scale, molecular dynamics (MD) provides a complementary means of examining nanocluster–surface interactions that are difficult to resolve experimentally, including relative interaction energetics, equilibrium interfacial organisation and surface mobility [18–20]. Previous simulations have demonstrated that Ag and Cu nanocluster behaviour is sensitive to graphene functionalisation and surface chemistry [18,19]. Such atomistic models operate at substantially smaller length scales than experimental nanoparticles and are most appropriately interpreted as comparative descriptions of interfacial behaviour rather than direct representations of experimentally observed particle assemblies. Multiscale modelling has increasingly been used to connect atomistic and electromagnetic descriptions of surface-enhanced spectroscopy [21], but quantitative integration with experimentally measured GO surface chemistry and nanoparticle organisation remains limited.

In this work, two commercial GO materials with contrasting measured surface oxygen contents, GO_{10} and GO_{30}, were investigated before and after PEG–NH_2 treatment and incorporation of Ag- and Cu-containing particles. FTIR, Raman, XPS, TGA, SEM, TEM and UV–Vis characterisation were combined with MD and FDTD simulations to relate surface chemistry, interfacial behaviour, nanoparticle organisation and optical response. The present study extends our previous experimental and MD work [4,18,19] by systematically comparing two GO surface-oxygen regimes and integrating quantitative nanoparticle-size and nearest-neighbour analyses with atomistic and experiment-informed electromagnetic modelling.

MD was used to compare nanocluster interaction energetics, interfacial organisation and dynamics across model graphene interfaces, while experimentally measured particle-size distributions and nearest-neighbour surface gaps established the structural regimes examined by controlled FDTD simulations. The principal contribution of this work is therefore the quantitative integration of GO surface chemistry and experimentally measured nanoparticle organisation with atomistic and electromagnetic modelling within a single multiscale structure–property framework. The FDTD calculations employ idealised metallic Ag and Cu reference structures to isolate size- and spacing-dependent optical effects and are not used to establish the chemical state of the experimental particles or experimentally demonstrated SERS performance.

2. Methodology

2.1. Materials and experimental preparation

2.1.1. Materials and nanocomposite preparation

Commercial oxidised graphene materials with contrasting surface oxygen contents, denoted GO_{10} and GO_{30}, were obtained from Sigma-Aldrich and NanoInnova Technologies, respectively. These designations are operational sample identifiers corresponding to the commercial materials used in this study and do not represent directly measured oxygen percentages. Four-arm amine-terminated polyethylene glycol hydrochloride (4arm-PEG5K-NH_2, HCl salt; average $M_n \approx 5000\ g \cdot mol^{-1}$), *N*-(3-dimethylaminopropyl)-*N*′-ethylcarbodiimide hydrochloride (EDC-HCl), *N*-hydroxysuccinimide (NHS), silver nitrate ($AgNO_3$) and trisodium citrate ($Na_3C_6H_5O_7$) were purchased from Sigma-Aldrich. Cu nanoparticles were obtained from CF Nanotechnology® (Suzhou, China). Ultrapure Milli-Q water was used throughout the experimental procedures unless otherwise stated.

GO modification and nanocomposite preparation followed our previously reported methodology [4]. PEG-NH_2 treatment was performed under EDC/NHS-mediated coupling conditions to prepare PEG-modified GO substrates. This terminology is used throughout the manuscript because the available characterisation supports PEG-associated surface modification but does not independently establish the fraction of PEG that is covalently attached. Ag nanoparticles were synthesised by citrate reduction of $AgNO_3$ using a Frens-type method adapted for Ag nanoparticles [22], with $AgNO_3$ as the precursor and trisodium citrate citrate ($Na_3C_6H_5O_7$) as the reducing and stabilising agent. Briefly, 50 mL of 1.0 mM $AgNO_3$ solution was heated under continuous stirring to boiling, after which 500 µL of 0.189 M $Na_3C_6H_5O_7$ was rapidly added. The mixture was maintained at boiling temperature and stirred at 200 rpm for a further 20 min. The resulting Ag nanoparticles were centrifuged at 2400 RCF for 30 min, resuspended in distilled water and stored at 4 °C in the dark until use.

GO and GO–PEG–NH_2 substrates were subsequently combined with Ag or Cu nanoparticles at a GO:NP mass ratio of 30:70 (w/w). The resulting nanocomposites were dispersed in water at a concentration of $1\ mg \cdot mL^{-1}$ and homogenised by combined sonication and mechanical stirring before characterisation.

2.1.2. Characterisation and quantitative image analysis

Morphology and nanoparticle organisation. Scanning electron microscopy (SEM) was performed using a JEOL JSM-6335F operated at 20 kV. Samples were mounted on conductive carbon tape before imaging. SEM micrographs were used to evaluate nanoparticle surface coverage, aggregation, particle-size distributions and spatial organisation. Transmission electron microscopy (TEM) was performed using a JEOL JEM-2100 operated at 200 kV. Samples were diluted to 0.01 wt% and drop-cast onto carbon-coated copper grids before analysis. TEM was used to examine nanoparticle morphology and association with the GO support.

Quantitative SEM image analysis was performed using ImageJ. Micrographs were calibrated using their corresponding scale bars and measurements were converted to physical dimensions before statistical analysis. Particle diameters were grouped into 10 nm intervals from 0 to 10 to > 90–100 nm, and the distributions were normalised to the total number of analysed particles for each condition. The analysed populations were $N = 54$, 74 and 204 for GO_{10}–Ag, GO_{30}–Ag and GO_{30}–PEG–NH_2–Ag, respectively, and $N = 84$, 112 and 654 for GO_{10}–Cu, GO_{30}–Cu and GO_{30}–PEG–NH_2–Cu, respectively.

Mean particle diameter and sample standard deviation were estimated from the grouped distributions using the midpoint of each 10 nm interval. The median diameter (D_{50}), D_{90}, and first and third quartiles were determined by linear interpolation within the corresponding size intervals, and the interquartile range was calculated as $IQR = Q_3 - Q_1$. Fractions of particles with diameters ≤ 20 nm, ≤30 nm and > 50 nm were calculated directly from the corresponding grouped particle counts.

Nearest-neighbour spatial organisation was quantified independently from the calibrated SEM data. For each resolved particle *i*, the projected area A_i and centroid coordinates were obtained, and an equivalent circular radius was calculated as

$$r_i = \sqrt{\frac{A_i}{\pi}} \tag{1}$$

The centre-to-centre distance between particle i and particle j was determined from

$$d_{ij} = \sqrt{(x_i - x_j)^2 + (y_i - y_j)^2} \quad (2)$$

and the nearest neighbour was identified from the minimum eligible centre-to-centre distance. The corresponding apparent surface-to-surface gap was calculated as

$$g_i = max\left[0, d_{ij} - (r_i + r_j)\right] \quad (3)$$

Image-edge objects and non-particle features associated with the GO substrate were excluded from the quantitative analysis. Negative calculated separations were assigned $g = 0$, representing apparent contact or overlap within the two-dimensional equivalent-particle representation. The resulting spacing distributions were expressed as empirical cumulative distribution functions (ECDFs) and characterised using the median gap, interquartile range, 90th-percentile gap (g_{90}) and fraction of apparent contacts ($g = 0$). Because SEM provides a two-dimensional projection of the nanoparticle arrangement, these measurements are reported as apparent nearest-neighbour surface gaps.

Surface chemistry. Fourier-transform infrared (FTIR) spectra were acquired using a Nicolet iS50 spectrometer equipped with a germanium attenuated total reflectance accessory. Spectra were recorded over 3700–700 cm^{-1} following background correction and were used to evaluate oxygen-containing functional groups and spectral changes associated with PEG–NH_2 treatment.

X-ray photoelectron spectroscopy (XPS) was performed using a monochromatic Al Kα source (hν = 1486.6 eV). Survey spectra were used to determine surface elemental composition and O/C ratios, while high-resolution C 1 s, O 1 s, N 1 s and selected S 2p spectra were analysed using CasaXPS. Shirley background subtraction and pseudo-Voigt GL (30) line shapes were applied using the minimum number of chemically justified components. Binding energies were referenced to the non-oxygenated C 1 s contribution at approximately 284.8 eV, and quantitative comparisons were based on survey-derived O/C ratios and relative high-resolution peak-area distributions.

XPS measurements were performed on GO_{10}, GO_{30} and their PEG–NH_2-modified derivatives to examine oxidation-dependent surface composition and changes associated with PEG treatment. The Ag- and Cu-containing nanocomposites were not analysed by XPS; consequently, the oxidation states of the metal-containing phases were not determined using this technique.

Raman spectra were acquired using a HORIBA 1250 M spectrometer equipped with a 532 nm diode-pumped solid-state laser, a 1200 gr mm^{-1} grating and a 400 μm slit. Measurements were performed using a 20 × objective with samples deposited on quartz substrates to minimise background interference. The degree of structural disorder was evaluated using the Raman D-to-G band intensity ratio (I_D/I_G), calculated from the baseline-corrected peak heights of the D and G bands at approximately 1350 and 1580 cm^{-1}, respectively.

Thermal analysis and apparent PEG-associated loading. Thermogravimetric analysis (TGA) and derivative thermogravimetric analysis (DTGA) were performed using a Seiko SSC 5200 TG-DTA 320 instrument. Approximately 10 mg of each sample was heated from 30 to 1000 °C at 10 °C · min^{-1} under helium. Prior to heating, the system was purged with helium at 100 mL · min^{-1} for 30 min.

Apparent PEG-associated loading was estimated from the additional mass loss of each PEG-treated material relative to its corresponding untreated GO over the 250–400 °C [23,24]:

$$L_{250-400} = W(250) - W(400) \quad (4)$$

$$W_{PEG,app} = L^{GO-PEG-NH_2}_{250-400} - L^{GO}_{250-400} \quad (5)$$

where $W(T)$ is the percentage mass remaining at temperature T. Values at 250 and 400 °C were obtained by linear interpolation between adjacent experimental points.

Robustness was assessed by independently varying the lower integration boundary between 240 and 260 °C and the upper boundary between 390 and 410 °C. A complementary analysis was performed after normalising each thermogram to its mass at 150 °C. The initial-mass-normalised values were retained as the primary analysis because the DTGA profiles did not show a common post-dehydration plateau at 150 °C for all samples, consistent with the complex multistep thermal decomposition behaviour of GO [25].

The TGA-derived values are therefore reported as apparent PEG-associated loadings rather than absolute surface grafting densities [24,26]. Because a neat PEG–NH_2 thermogram acquired under identical conditions was unavailable, no correction was applied for PEG decomposition outside the selected temperature interval. Conversion to a grafting density in chains nm^{-2} was not attempted because no reliable experimental specific surface area was available to normalise the polymer loading by surface area [23]. Moreover, TGA alone cannot distinguish covalently bound PEG from non-covalently retained or physically entrapped/intercalated material [24]. The calculated values therefore quantify the amount of PEG-associated material, rather than its mode of attachment. As one thermogram was analysed for each composition, replicate standard deviations are not reported.

Optical characterisation. UV–Vis spectra were recorded using a Thorlabs SLS205 fibre-coupled xenon light source over 200–1000 nm using 10 mm quartz cuvettes. The spectra were used to evaluate the optical response of the nanocomposites and identify plasmonic absorption features where resolvable.

2.2. Atomistic modelling of GO-Nanocluster interactions

2.2.1. Model construction and simulation parameters

Molecular dynamics (MD) simulations were performed to investigate how graphene surface chemistry influences nanocluster interfacial organisation, interaction energetics and mobility. The model series comprised pristine graphene (PG), GO_{10}, GO_{30} and PEG-modified GO_{30} (GO_{30}–PEG–NH_2), with Cu_{13} and Ag_{13} nanoclusters used as atomistic probes of metal–surface interactions.

The GO_{10} and GO_{30} atomistic models had stoichiometric O/C ratios of 0.163 and 0.315, respectively, compared with experimentally determined XPS values of 0.048 and 0.522 (Section 3.1.2 and Table S2). Although the models preserve the progression from lower to higher oxidation, they do not reproduce the absolute experimental compositions or the magnitude of their difference. Accordingly, the GO_{10} and GO_{30} models are treated as qualitative low- and high-oxidation analogues for comparing oxidation-dependent interfacial behaviour rather than as compositionally exact representations of the experimental materials.

Graphene sheets of 36 × 36 $Å^2$ were constructed for all systems. GO_{10} ($C_{196}H_{47}O_{32}$) and GO_{30} ($C_{200}H_{61}O_{63}$) corresponded to oxygen contents of 17.57 and 29.03 wt%, respectively, with hydroxyl, epoxy and carboxyl groups distributed according to established protocols [18]. PEG modification was represented by four amine-terminated PEG chains with a degree of polymerisation of 10 attached to the GO_{30} model. This construction represents the PEG-containing computational interface and does not define the bonding mode of PEG in the experimental material.

Icosahedral Cu_{13} and Ag_{13} nanoclusters were initially positioned 12 Å above the substrate within a 40 × 40 × 40 $Å^3$ periodic simulation cell containing 2375 explicit water molecules (Fig. 1). Their characteristic dimensions were approximately 5.65 and 6.85 Å, respectively. These clusters are substantially smaller than the experimentally observed nanoparticles and were therefore used as comparative probes of surface-chemistry effects on interfacial organisation and mobility rather than to reproduce the full particle geometry, curvature or faceting of the experimental systems.

All systems were energy-minimised and equilibrated before production simulations. Calculations were performed using the Forcite module in Materials Studio under the NVT ensemble at 298 K with a

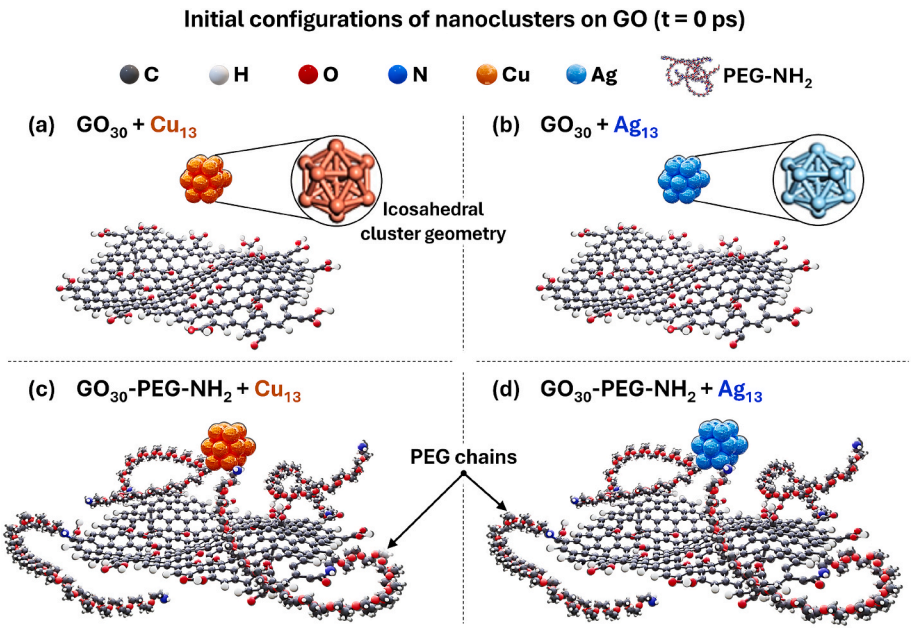


Fig. 1. Representative initial atomistic configurations used in the MD simulations of Cu_{13} and Ag_{13} nanoclusters on graphene-based substrates. (a,b) GO_{30} systems and (c,d) corresponding GO_{30}–PEG–NH_2 systems at $t = 0$ ps. Nanoclusters were initially positioned 12 Å above the substrate. Water molecules and periodic simulation-cell boundaries are omitted for clarity.

Nosé–Hoover thermostat [27,28].

Non-covalent interactions were described using the COMPASSII force field with a cut-off distance of 12.5 Å. COMPASS force-field parameters are developed within a consistent parameterisation framework intended to support simulations involving mixed material classes [29]. However, the specific parameterisation and validation of the Cu and Ag terms employed by the Materials Studio implementation could not be independently verified for the present metal–GO interfaces. Moreover, COMPASSII is non-reactive and does not explicitly describe charge transfer, chemisorption or oxidation processes that may occur at metal–oxygen interfaces. Consequently, the simulations were used to evaluate relative changes in nanocluster interaction energetics, interfacial organisation and mobility across the different surface models, rather than to provide quantitatively validated metal–surface binding energies.

Production trajectories were run for 1000 ps. Interaction-energy and equilibrium structural analyses were based on the final 300 ps following equilibration, whereas the MSD analysis used the trajectory interval specified below. As one production trajectory was available for each system, the energetic and mobility metrics are interpreted as comparative descriptors rather than statistically converged ensemble averages. GO_{10}–PEG–NH_2 was not included in the MD series; therefore, PEG-induced effects are assessed for GO_{30} only and are not used to infer oxidation-dependent PEG responses across both GO oxidation levels.

2.2.2. Interaction energetics and nanocluster dynamics

Interaction energetics were evaluated to compare the effects of surface oxidation and PEG modification on nanocluster–substrate interactions. The interaction-energy descriptor, ΔE, was calculated as

$$\Delta E = E_{\mathrm{GO+water+cluster}} - (E_{\mathrm{GO+water}} + E_{\mathrm{cluster}}) \tag{6}$$

where $E_{\mathrm{GO+water+cluster}}$ is the potential energy of the complete hydrated system, $E_{\mathrm{GO+water}}$ is the energy of the corresponding hydrated graphene-based substrate containing the same number of water molecules as the complete system, and E_{cluster} is the energy of the isolated nanocluster. Interaction energies were averaged over the final 300 ps of the respective trajectories. More negative ΔE values indicate a more favourable interaction within this comparative framework. Retaining the same number of water molecules in the complete and substrate-reference systems provides a consistent solvent background; however, because the reference state contains the hydrated substrate and an isolated nanocluster, ΔE also incorporates contributions associated with cluster hydration and solvent reorganisation. It is therefore interpreted as a hydrated-system interaction-energy descriptor rather than an adsorption free energy or intrinsic metal–surface binding energy.

Incremental differences, ΔΔE, were calculated for PG → GO_{10}, GO_{10} → GO_{30} and GO_{30} → GO_{30}–PEG–NH_2 to compare energetic changes across the model series. Because PEG modification introduces additional interacting atoms, the GO_{30} and GO_{30}–PEG–NH_2 interaction energies were additionally normalised by the estimated nanocluster–substrate contact area. The interfacial contact area was evaluated frame-by-frame over the final 300 ps of each production trajectory using the solvent-accessible surface areas (SASA) of the isolated nanocluster, isolated graphene-based substrate and combined nanocluster–substrate interface. For each frame, the contact area was calculated as

$$A_{\mathrm{contact}} = \frac{SASA_{\mathrm{cluster}} + SASA_{\mathrm{surface}} - SASA_{\mathrm{complex}}}{2} \tag{7}$$

and the resulting contact areas were averaged over the final 300 ps. The area-normalised interaction energy was then calculated as

$$\Delta E_A = \frac{\Delta E}{A_{\mathrm{contact}}} \tag{8}$$

where A_{contact} is the estimated interfacial contact area in $Å^2$. This normalisation was applied to the GO_{30} and GO_{30}–PEG–NH_2 systems to assess whether the energetic difference associated with PEG modification persisted after accounting for differences in nanocluster contact area.

Interfacial organisation was assessed using radial distribution functions (RDFs) between the nanocluster centre of mass (COM) and the graphene-based surface. Nanocluster mobility was quantified from the COM mean squared displacement (MSD):

$$\mathrm{MSD}(t) = \langle |r_{\mathrm{COM}}(t) - r_{\mathrm{COM}}(0)|^2 \rangle \tag{9}$$

where $r_{\mathrm{COM}}(t)$ and $r_{\mathrm{COM}}(0)$ denote the COM positions at time t and at the beginning of the analysed trajectory, respectively. MSD profiles were fitted over 0–495 ps using 100 points sampled at 5 ps intervals according

to

$$\mathrm{MSD}(t) = K_\alpha \bullet t^\alpha \tag{10}$$

where K_α is the generalised transport coefficient ($\text{Å}^2 \cdot \text{ps}^{-\alpha}$) and α is the anomalous-scaling exponent. Parameters were obtained by unweighted nonlinear least-squares regression using curve_fit in SciPy, with $K_\alpha > 0$ and $0 \leq \alpha \leq 2$. Values of $0 < \alpha < 1$, $\alpha = 1$ and $\alpha > 1$ were classified as apparent subdiffusive, normal-diffusive and superdiffusive scaling, respectively, describing MSD temporal scaling without assigning a specific microscopic transport mechanism.

Fit quality was assessed using R^2 on the linear MSD scale. Because K_α depends on α, both parameters were interpreted jointly rather than treating K_α as a conventional diffusion coefficient. Formal parameter uncertainties were obtained from the nonlinear-regression covariance matrix and represent fitting precision rather than variability between independent trajectories. The anomalous-diffusion fitting procedure followed the approach previously established for related Cu/Ag–graphene systems [18]. The same analysis was applied to the previously reported GO_{30}–Cu and GO_{30}–Ag MSD datasets [4] to obtain the corresponding K_α and α parameters, without generating additional MD trajectories.

2.3. Numerical modelling of plasmonic response and electromagnetic enhancement

2.3.1. FDTD geometry and Experiment-Informed parameterisation

Finite-difference time-domain (FDTD) simulations, based on the standard Yee formulation [30], were performed using Ansys Lumerical FDTD Solutions. The modelling comprised three stages: isolated-particle size sweeps, controlled dimer-gap analyses and experiment-informed heterogeneous assemblies, allowing particle-size and spacing effects to be linked to the experimentally measured morphology.

Spherical Ag and Cu nanoparticles were modelled on a 3 nm GO support in an aqueous medium ($n = 1.33$). The spherical geometry was adopted as a controlled modelling approximation to isolate the effects of particle size and interparticle separation. It does not reproduce the full morphological heterogeneity of the experimentally observed nanoparticles; therefore, the simulated optical response is interpreted primarily in terms of relative trends rather than as an exact representation of individual experimental particles. Wavelength-dependent optical constants were used for Ag and Cu [31] and for GO [32], including GO absorption and damping. The reported GO optical constants were used as an effective continuum representation of the support to incorporate wavelength-dependent absorption and damping. This approximation does not reproduce local variations associated with GO thickness, wrinkling or anisotropy, and the calculated response is therefore interpreted comparatively rather than as an exact optical representation of individual GO flakes. The metallic Ag/Cu optical models describe the electromagnetic response and do not establish the chemical state of the experimental metal-containing phases.

Particle-size effects were evaluated for diameters of 10, 20, 30, 50, 80 and 100 nm, spanning the principal experimental size distributions. Interparticle coupling was examined using 20 nm dimers with metal surface-to-surface gaps, g_{metal}, of 5, 10, 20, 50, 100 and 200 nm, together with an isolated-particle reference. The electric field was polarised along the dimer axis. This gap range probes the close-separation regime identified from the SEM nearest-neighbour distributions; apparent $g = 0$ contacts in the two-dimensional SEM analysis were not treated as classical zero-width optical junctions.

PEG thickness was treated as a modelling parameter because it was not independently resolved experimentally. Sensitivity calculations were performed for $t_{\mathrm{PEG}} = 0$, 3, 5, 7 and 10 nm ($n_{\mathrm{PEG}} = 1.46$) [33] using 20 nm dimers at fixed $g_{\mathrm{metal}} = 20$ nm. Across this range, λ_{LSPR} shifted by no more than 8.75 nm and the maximum $|E/E_0|$ changed by no more than approximately 11.5%, indicating that the principal coupling trends were not dominated by the assumed shell thickness (Fig. S4; Table S9).

Experiment-informed assemblies containing nine nanoparticles were additionally constructed for the GO_{10}, GO_{30} and GO_{30}–PEG–NH_2 Ag and Cu systems using representative particle sizes and spatial arrangements derived from the SEM analysis. These models represent controlled local morphologies rather than exact SEM reconstructions. A 700 × 700 × 3 nm GO support was used for the assembly calculations. The overall FDTD geometry, illumination conditions and controlled dimer parameters are summarised schematically in Fig. 2.

2.3.2. Excitation, boundary conditions and mesh convergence

Controlled particle and dimer simulations employed a total-field scattered-field (TFSF) source, while the heterogeneous assemblies were illuminated by a normally incident plane wave propagating along $-z$, with $E \| x$. Perfectly matched layer (PML) boundaries were applied to represent an open electromagnetic domain, and broadband calculations were performed over 300–1000 nm.

Mesh convergence was evaluated by progressive refinement from 2 to 0.25 nm for representative single-particle simulations and from 1 to 0.25 nm for the close-gap dimer geometry. A 0.5 nm local mesh was retained for production calculations after comparison with the 0.25 nm reference. For the tested single-particle and dimer geometries, the LSPR position was unchanged between the 0.5 and 0.25 nm meshes, while residual differences in peak extinction efficiency and maximum near-field amplitude remained within approximately 5.3% and 8.3%, respectively. Because the electromagnetic enhancement metric scales as $EF_{\mathrm{EM}} = |E/E_0|^4$, its numerical sensitivity was additionally evaluated as a function of mesh size at fixed common wavelengths for the 5 nm Ag and Cu dimers. The complete convergence analysis, including the EF_{EM}-versus-mesh-size plots, is provided in Fig. S3 and Table S8.

2.3.3. Optical response and electromagnetic enhancement metrics

Extinction, absorption and scattering cross-sections were related by

$$C_{\mathrm{ext}} = C_{\mathrm{abs}} + C_{\mathrm{sca}} \tag{11}$$

where C_{ext}, C_{abs} and C_{sca} are the extinction, absorption and scattering cross-sections, respectively.

For controlled particle and dimer comparisons, extinction efficiency (Q_{ext}) was normalised by the corresponding projected metal area. For the experiment-informed nine-particle assemblies, Q_{ext} was normalised by the sum of the projected areas of the individual metal nanoparticles, $\sum_i \pi (D_i/2)^2$, excluding any PEG shell. The dominant extinction maximum defined the localised surface plasmon resonance wavelength, λ_{LSPR}, and resonance quality was calculated as

$$Q_{\mathrm{res}} = \frac{\lambda_{\mathrm{LSPR}}}{\mathrm{FWHM}} \tag{12}$$

where FWHM is the full width at half maximum of the corresponding extinction resonance. The relative absorption and scattering contributions at λ_{LSPR} were evaluated from $C_{\mathrm{abs}}/C_{\mathrm{ext}}$ and $C_{\mathrm{sca}}/C_{\mathrm{ext}}$, respectively.

Local field enhancement was quantified from the normalised electric-field amplitude,

$$F(\mathbf{r}) = \left| \frac{E(\mathbf{r})}{E_0} \right| \tag{13}$$

where $E(\mathbf{r})$ and E_0 are the local and incident electric-field amplitudes. For the experiment-informed assemblies, field maps were evaluated at each model's λ_{LSPR} on planes at z = 5, 15, 30, 50 and 85 nm. The maximum sampled-plane $|E/E_0|$ was used to compare near-field localisation among the six assemblies. The minimum three-dimensional metal surface-to-surface separation, g_{min}, was calculated from the particle coordinates and used to examine the relationship between local particle organisation and electromagnetic enhancement. The corresponding structural and optical summary is provided in Table S10, with the complete Ag and Cu assembly geometries given in Table S11 and S12.

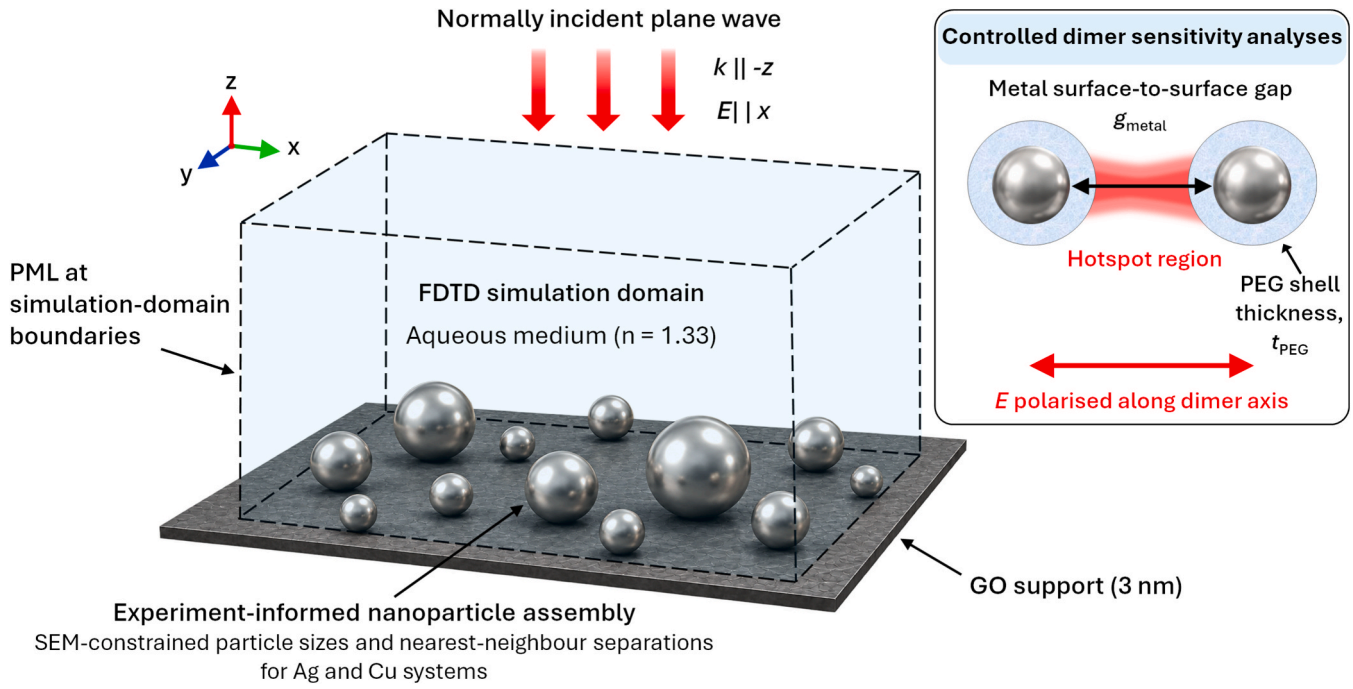


Fig. 2. Schematic of the FDTD modelling framework for GO-supported Ag and Cu nanoparticle assemblies. Experiment-informed particle sizes and nearest-neighbour separations were represented on a 3 nm GO support within an aqueous medium ($n = 1.33$) and illuminated by a normally incident plane wave ($k \| -z$, $E \| x$) with perfectly matched layer (PML) boundaries. The inset shows the controlled dimer sensitivity model used to evaluate the effects of metal surface-to-surface gap (g_{metal}) and PEG-shell thickness (t_{PEG}) on localised electromagnetic hotspot formation. Schematic not to scale.

The local electromagnetic enhancement associated with the electromagnetic component of SERS was estimated using the conventional fourth-power approximation [34,35]:

$$EF_{EM} \approx \left|\frac{E}{E_0}\right|^4 \tag{14}$$

where EF_{EM} was calculated from the maximum $|E/E_0|$ evaluated at the corresponding λ_{LSPR}. For the experiment-informed assemblies, EF_{EM} was calculated from the maximum sampled-plane $|E/E_0|$ across the evaluated heights. EF_{EM} is reported as a predicted local electromagnetic enhancement metric, rather than an experimentally measured SERS enhancement factor or a spatially averaged enhancement. The fourth-power approximation assumes similar local-field enhancement at the excitation and Raman-shifted wavelengths and accounts only for the electromagnetic contribution; chemical or charge-transfer enhancement is not included. Collectively, λ_{LSPR}, C_{ext}, Q_{res}, absorption/scattering partitioning, $|E/E_0|$ and EF_{EM} were used to evaluate the effects of nanoparticle size, metal-to-metal separation, PEG-shell thickness and experiment-informed particle organisation on the predicted plasmonic response.

3. Results and Discussion

3.1. Surface chemistry and structural evolution of graphene oxide

3.1.1. Chemical and structural evolution following oxidation and PEG–NH_2 functionalisation

The influence of oxidation level and subsequent PEG–NH_2 treatment on GO surface chemistry and structure was examined using complementary FTIR and Raman spectroscopy (Fig. 3). The FTIR spectra (Fig. 3a; Table S1) show oxygen-containing vibrational features in both GO_{10} and GO_{30}, although these contributions are comparatively weak in GO_{10}. GO_{10} exhibits weak features at approximately 1710 cm^{-1} and within the C–O/C–O–C region, consistent with a relatively limited population of carbonyl and oxygen-containing functionalities. In comparison, GO_{30} exhibits a broader O–H stretching band near 3400 cm^{-1}, a stronger carbonyl feature at approximately 1729 cm^{-1} and greater absorption within the 1000–1300 cm^{-1} region, consistent with its higher degree of oxidation [36]. The broad contribution near 1600 cm^{-1} may contain overlapping C=C skeletal and H_2O bending vibrations, while weaker C–H out-of-plane features between approximately 700 and 900 cm^{-1} indicate retention of graphitic domains following oxidation [36,37]. These FTIR observations are used to identify functional-group environments and comparative spectroscopic trends, whereas quantitative surface composition and O/C ratios are obtained from XPS in Section 3.1.2.

PEG–NH_2 treatment produces additional spectral changes in both oxidation states. C–H stretching features between approximately 2800 and 3000 cm^{-1} are observed in the treated materials, consistent with PEG-associated aliphatic groups. GO_{30}–PEG–NH_2 additionally exhibits features at approximately 1670 and 1538 cm^{-1} within the Amide I and Amide II regions, respectively, together with pronounced absorption in the ether-rich C–O/C–O–C region. These changes are more evident than those observed for GO_{10}–PEG–NH_2 and are consistent with a greater extent of PEG-associated surface modification on GO_{30} [4]. However, these FTIR features do not independently establish covalent amidation. When considered together with the XPS and TGA results presented in Sections 3.1.2 and 3.3, they support the retention of PEG-associated material following reaction and purification, with a greater relative amount associated with GO_{30}. The available measurements cannot distinguish the relative contributions of EDC/NHS-mediated covalent coupling, non-covalent retention and physical entrapment or intercalation.

Raman spectroscopy provides complementary information on structural changes accompanying oxidation and PEG–NH_2 treatment (Fig. 3b). All samples exhibit the characteristic D and G bands at approximately 1350 and 1580 cm^{-1}, respectively, together with a weaker 2D contribution near 2700 cm^{-1}. The baseline-corrected peak-height I_D/I_G ratios lie between approximately 0.95 and 1.00, demonstrating measurable but relatively modest differences in the defect-sensitive D-to-G response across the four materials. The changes

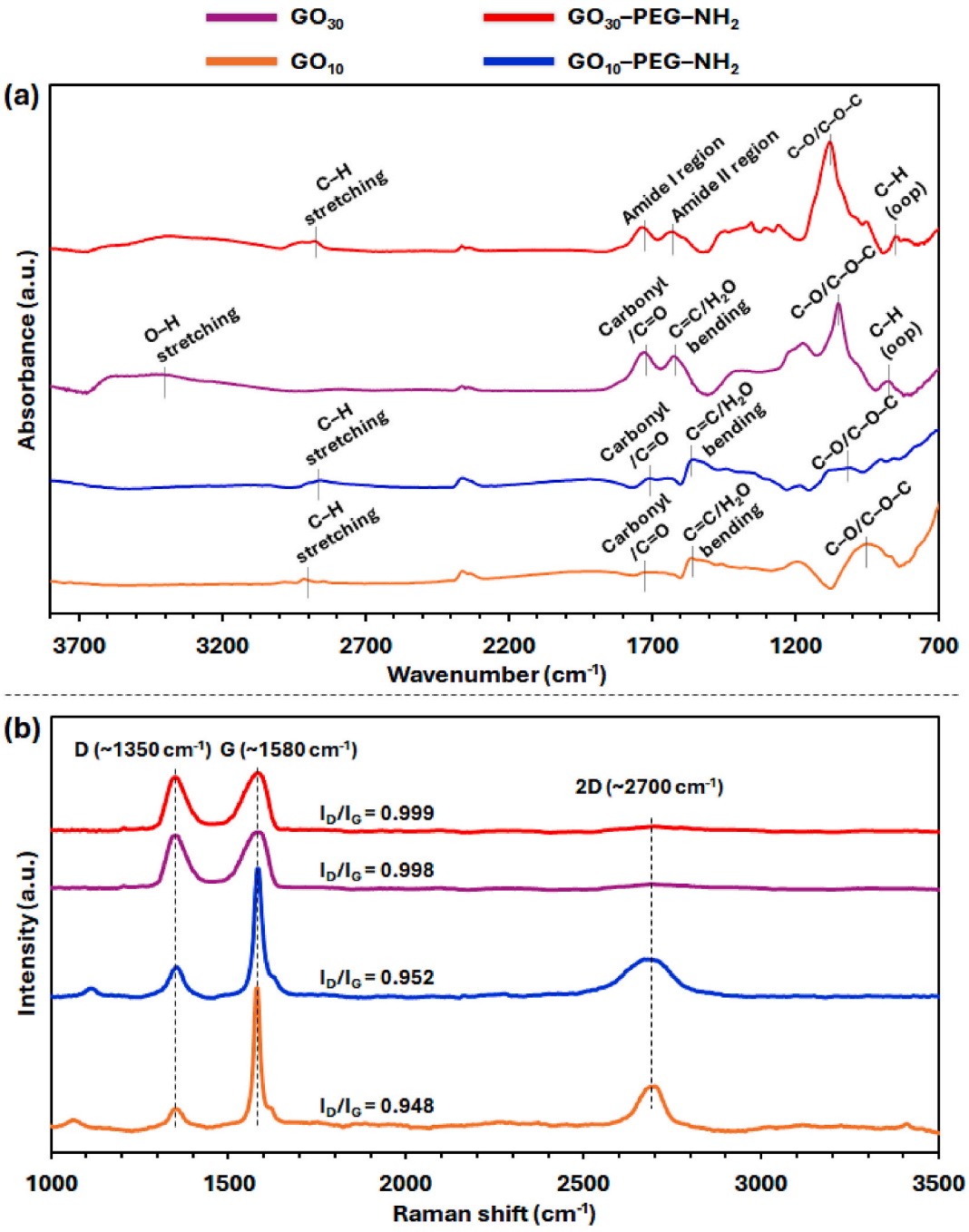


Fig. 3. (a) FTIR and (b) Raman spectra of GO_{10}, GO_{30} and their PEG–NH_2-treated counterparts. FTIR shows more pronounced oxygen-containing functionalities in GO_{30} and PEG-associated spectral changes following treatment, particularly for GO_{30}–PEG–NH_2. Raman spectra show changes in the D-to-G band intensity ratio I_D/I_G and attenuation of the 2D band, consistent with differences in graphitic ordering and structural perturbation across the GO systems. The 2D-band changes are not interpreted as direct evidence of changes in flake thickness.

observed following PEG–NH_2 treatment should therefore not be regarded as negligible; rather, they indicate that surface treatment is accompanied by detectable perturbation of the graphitic structure, although the magnitude of the change remains small relative to the overall D and G responses. Because I_D/I_G is sensitive to the defect structure and organisation of sp^2 domains, these variations are interpreted comparatively rather than as a direct quantitative measure of defect concentration [36].

Changes are also evident in the 2D region. The 2D contribution becomes weak or strongly attenuated in the more structurally perturbed spectra. Although the intensity and profile of the 2D band can be sensitive to layer number in comparatively ordered graphene, the present materials are oxidised and structurally disordered GO systems. Consequently, attenuation of the 2D band is not interpreted here as direct evidence of a change in GO flake thickness. Instead, it is considered alongside the D and G responses as evidence of changes in graphitic ordering and the electronic environment associated with oxidation and subsequent surface treatment [36]. Direct determination of flake thickness would require an independent thickness-sensitive measurement and was not performed in the present study.

Collectively, the FTIR and Raman results demonstrate clear chemical and structural differences between the two GO substrates and further changes following PEG–NH_2 treatment. FTIR indicates a greater abundance of oxygen-containing functionalities in GO_{30} and more

pronounced PEG-associated spectral changes following treatment, while Raman confirms corresponding perturbations of the carbon framework without providing independent evidence for changes in flake thickness. Together with the quantitative XPS and TGA analyses presented below, these observations establish the surface-chemical differences used to examine how oxidation and PEG-associated modification influence subsequent nanoparticle organisation.

3.1.2. Quantitative surface composition and chemical environments (XPS)

XPS was used to quantify differences in surface composition between GO_{10} and GO_{30} and to examine changes following PEG–NH_2 treatment. Survey spectra (Fig. S1; Table S2) show a pronounced difference in initial oxidation state, with the surface O/C ratio increasing from 0.048 for GO_{10} to 0.522 for GO_{30}. Following PEG–NH_2 treatment, the O/C ratio increases from 0.048 to 0.123 for GO_{10} but decreases from 0.522 to 0.444 for GO_{30}. This contrasting response is consistent with their different initial compositions. Because the PEG backbone contains approximately two carbon atoms per ether oxygen, a PEG-associated contribution can increase the O/C ratio of oxygen-poor GO_{10} while lowering the apparent ratio of highly oxidised GO_{30}. As XPS atomic percentages are normalised and surface-sensitive, these changes indicate modification of the sampled surface composition but do not directly quantify PEG loading, demonstrate GO deoxygenation or establish the PEG–GO bonding mechanism.

Trace nitrogen was present in untreated GO_{10} and GO_{30} (0.51 and 1.20 at. %, respectively) and decreased following PEG–NH_2 treatment to 0.29 and 0.73 at. %, respectively. Given its presence before treatment and the absence of an increase afterwards, the N 1 s signal cannot be assigned specifically to PEG-derived nitrogen or used as evidence of amide formation. High-resolution N 1 s spectra of GO_{30} and GO_{30}–PEG–NH_2 are therefore provided in Fig. S2 for completeness. Although fitting indicates a redistribution of the N 1 s envelope following treatment, the low nitrogen abundance and pre-existing nitrogen in untreated GO_{30} preclude assignment of these changes specifically to PEG incorporation or covalent amidation.

C 1 s Analysis.

The high-resolution C 1 s spectra (Fig. 4; Table S3) were fitted using C=C, C–C/C–H, C–O, C=O/N–C=O and O–C=O components [36,38]. C=C and C–C/C–H were grouped as non-oxygenated carbon, with the remaining components classified as oxygenated carbon for cross-sample comparison. The low-binding-energy components were resolved separately where supported by the spectra, whereas a combined C=C/C–C/C–H contribution was used for GO_{30}. The C=O/N–C=O region was treated as an unresolved carbonyl contribution and was not used as evidence of amide formation, as the N 1 s data do not independently support this assignment.

GO_{10} is dominated by non-oxygenated carbon (93.42%), with oxygenated components accounting for only 6.58% of the fitted C 1 s

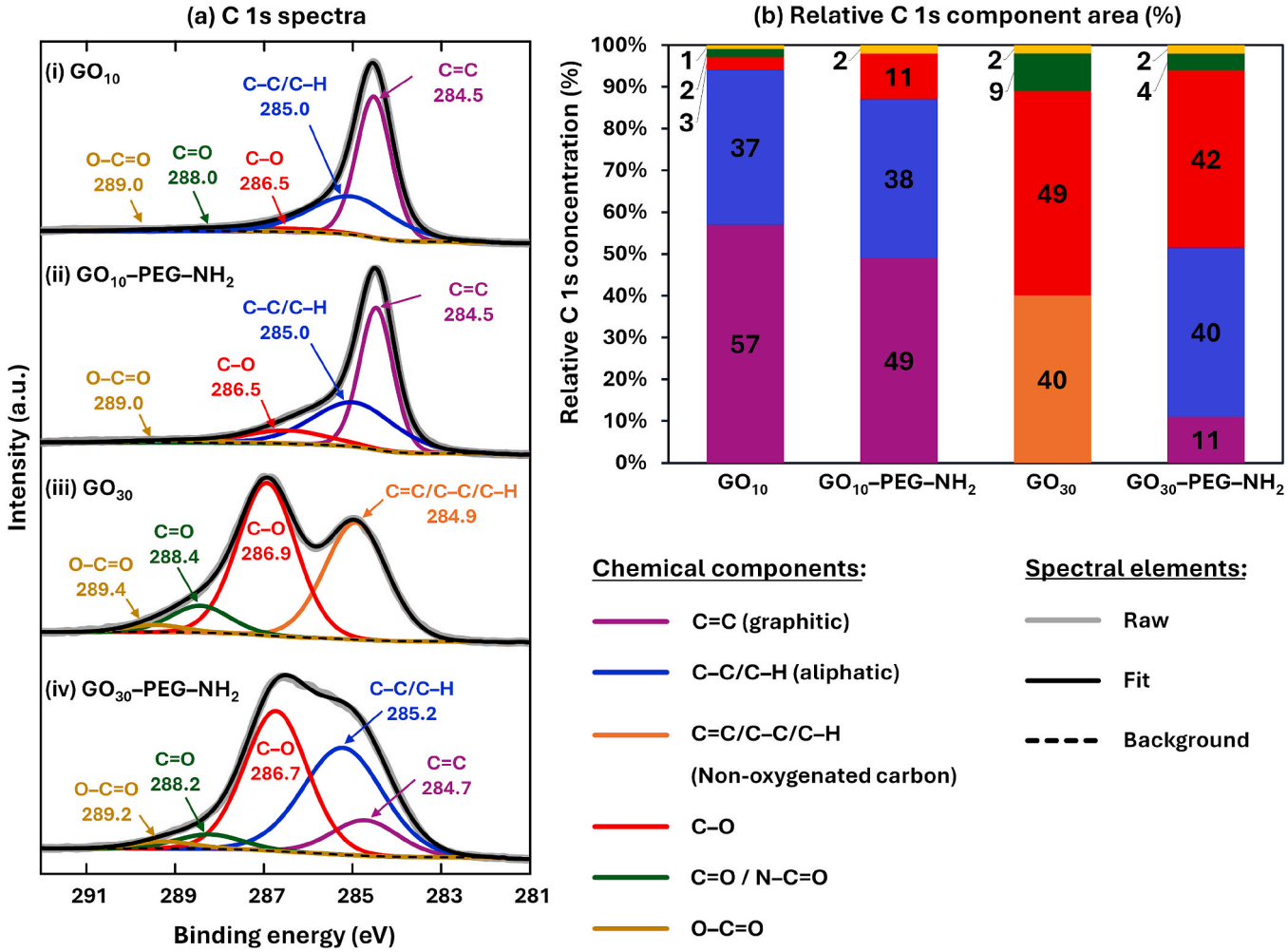


Fig. 4. High-resolution C 1 s XPS spectra and quantitative analysis of GO_{10}, GO_{30} and their PEG–NH_2-treated counterparts. (a) Deconvoluted C 1 s spectra showing experimental data (grey), fitted envelopes (black) and components assigned to C=C (sp^2), C–C/C–H (sp^3), combined non-oxygenated carbon (C=C/C–C/C–H), C–O, C=O/N–C=O and O–C=O environments. (b) Relative C 1 s component areas showing the substantially greater oxygenated-carbon contribution in GO_{30} and redistribution of carbon environments following PEG–NH_2 treatment.

envelope. In contrast, oxygenated carbon accounts for 59.88% of GO_{30}, including a dominant C–O contribution of 48.98%. This difference agrees with the survey-derived O/C ratios and confirms the substantially greater abundance of oxygen-containing carbon environments in GO_{30}.

Following PEG–NH_2 treatment, the C–O contribution in GO_{10} increases from 3.31% to 11.13%, while non-oxygenated carbon decreases from 93.42% to 86.83%, consistent with enrichment of the sampled surface in C–O/C–O–C environments. For GO_{30}–PEG–NH_2, the non-oxygenated contribution increases from 40.12% to 51.72%, while C–O remains a major component at 41.87%. These different responses reflect the markedly different starting compositions and demonstrate redistribution of carbon environments following treatment. The component near 285.2 eV is assigned generally to non-oxygenated/aliphatic C–C/C–H and is not considered a specific PEG marker, as most PEG-backbone carbon is directly bonded to oxygen and contributes predominantly to the C–O/C–O–C region near 286.5–286.7 eV. The C 1 s changes therefore support PEG-associated modification of the sampled surface but do not establish the bonding configuration of the retained material.

O 1 s Analysis.

The O 1 s spectra (Fig. 5; Table S4) provide complementary information on oxygen-containing surface environments. Component areas represent relative contributions within each fitted O 1 s envelope rather than elemental oxygen concentrations, which were determined from the survey spectra.

GO_{10} exhibits a dominant C–O contribution (72.41%), associated with hydroxyl, ether and epoxide environments, together with carbonyl oxygen (27.59%). GO_{30} similarly contains predominantly C–O environments (79.44%), accompanied by carbonyl oxygen (12.13%) and a higher-binding-energy contribution (8.43%) that may include hydroxyl groups, adsorbed/interlayer water and single-bond oxygen associated with carboxyl species [36]. Although the relative C–O fractions within the fitted envelopes are similar, the survey O/C ratios establish the substantially greater overall surface oxygen abundance of GO_{30}.

Following PEG–NH_2 treatment, GO_{10}–PEG–NH_2 contains 56.55% C–O and 37.05% higher-binding-energy oxygen, indicating redistribution of the sampled oxygen environments. The minor low-binding-energy contribution (6.41%) is interpreted cautiously because Al detected in the corresponding survey spectrum may contribute through Al–O and/or Al–OH environments. For GO_{30}–PEG–NH_2, C–O accounts for 93.10% of the fitted envelope, while carbonyl and higher-binding-energy contributions decrease to 3.52% and 3.37%, respectively. The dominance of C–O environments is consistent with an increased relative contribution from ether-rich PEG-associated material. However, because these fractions are normalised within each O 1 s envelope, the changes may also reflect attenuation of the underlying GO response and cannot independently demonstrate removal or conversion of specific GO oxygen functionalities.

Collectively, the survey, C 1 s and O 1 s analyses establish the distinct surface chemistries of GO_{10} and GO_{30} and their compositional changes following PEG–NH_2 treatment. Together with FTIR (Section 3.1.1) and TGA (Section 3.3), these results support retention of PEG-associated material after reaction and purification, with a greater relative extent of modification for GO_{30}–PEG–NH_2. However, the N 1 s response does not independently support amide formation, and the absence of a PEG–NH_2-treated control prepared without EDC/NHS prevents differentiation between covalent coupling, non-covalent retention and

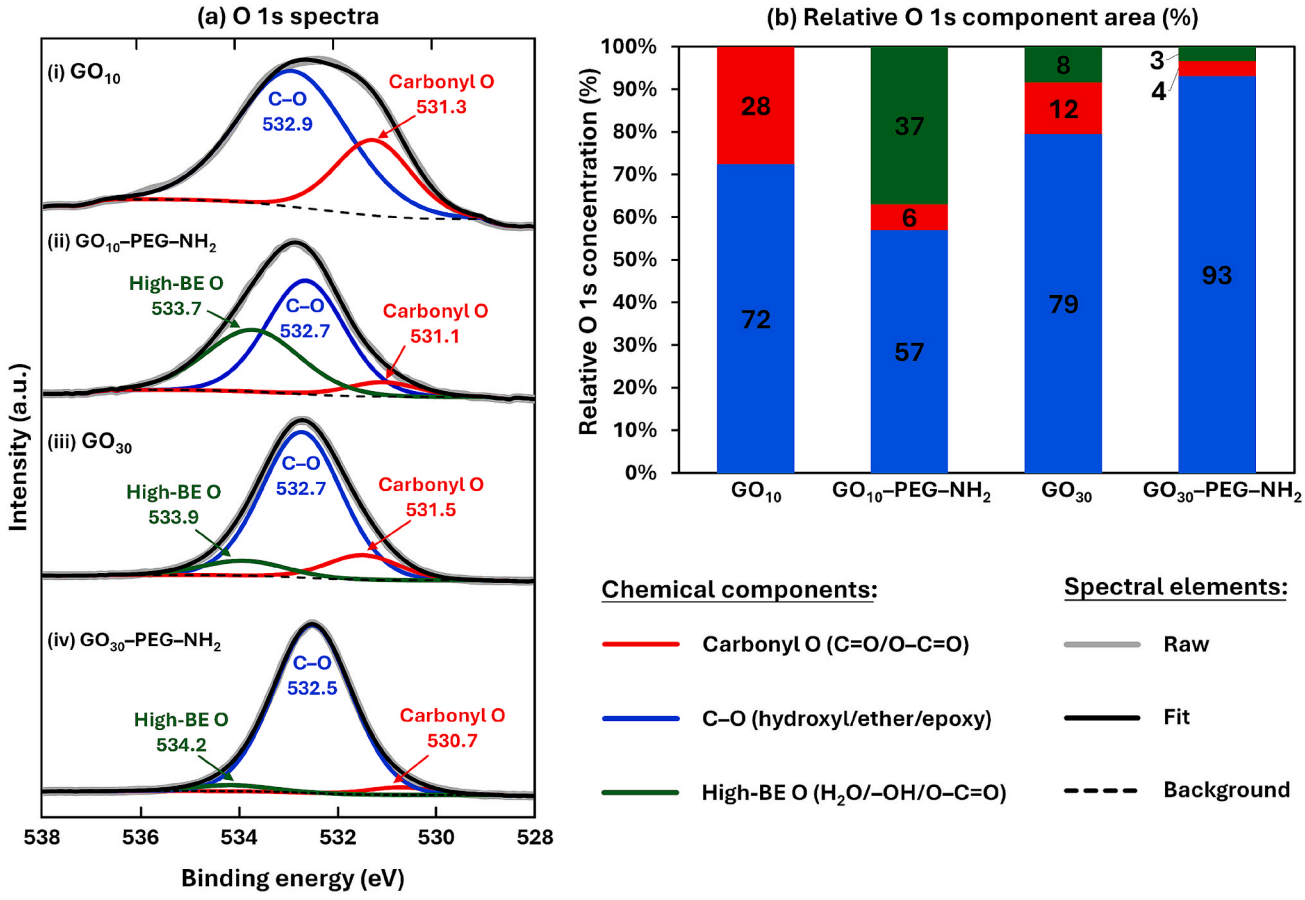


Fig. 5. High-resolution O 1 s XPS spectra and quantitative analysis of GO_{10}, GO_{30} and their PEG–NH_2-treated counterparts. (a) Deconvoluted O 1 s spectra showing experimental data (grey), fitted envelopes (black) and components assigned to carbonyl oxygen (C=O/O–C=O), C–O environments (hydroxyl/ether/epoxy) and higher-binding-energy oxygen environments. (b) Relative O 1 s component areas showing differences in oxygen-containing surface environments with oxidation and their redistribution following PEG–NH_2 treatment.

physical entrapment/intercalation. The combined evidence therefore supports oxidation-dependent PEG-associated surface modification without establishing a specific PEG–GO bonding mechanism. This difference produces chemically distinct interfacial environments for subsequent nanoparticle incorporation, providing the surface-chemical basis for examining the changes in particle organisation described in Section 3.2.

3.2. Nanoparticle Dispersion and interfacial structural control

3.2.1. SEM/EDS and Particle-Size distributions

SEM and EDS analyses (Fig. 6) reveal systematic changes in Ag- and Cu-containing nanoparticle organisation with increasing GO oxidation and subsequent PEG–NH_2 treatment. Relative to GO_{10}, GO_{30} exhibits fewer large agglomerated features and more homogeneous particle coverage, particularly for Cu, while PEG–NH_2 treatment further shifts the morphology towards smaller particulate features. These changes are consistent with the surface-chemistry differences established in Section 3.1 and with previous observations of nanoparticle organisation on modified GO interfaces [4,39].

Representative local EDS analyses (Fig. 6a–f) confirm the presence of Ag or Cu in the corresponding nanocomposites. EDS is used for elemental identification only and does not establish particle oxidation state or crystalline phase; the oxygen signal also includes contributions from the GO substrate and PEG-modified interface and therefore cannot be assigned specifically to metal oxides.

The normalised particle-size distributions (Fig. 6g,h) quantitatively support the SEM observations. For Cu, mean particle diameter decreases from 31.8 ± 28.5 nm for GO_{10}–Cu to 23.0 ± 24.7 nm for GO_{30}–Cu and 14.8 ± 18.2 nm for GO_{30}–PEG–NH_2–Cu, accompanied by decreases in D_{50} from 22.5 to 10.7 and 7.8 nm and in D_{90} from 77.2 to 64.5 and 39.5 nm. The fraction ≤ 20 nm correspondingly increases from 47.6% to 62.5% and 78.7%. Ag exhibits the same, although less pronounced, progression: mean diameter decreases from 34.8 ± 28.2 to 30.7 ± 27.0 and 27.2 ± 25.8 nm, while D_{50} decreases from 28.3 to 22.5 and 17.3 nm. Complete particle-size statistics are provided in Table S5.

Nearest-neighbour analysis shows that these changes reflect redistribution of particle organisation rather than a simple increase in separation. For Ag, the median apparent surface-to-surface gap changes from 0.661 to 0.230 and 0.424 μm, while the apparent contact/overlap fraction ($g = 0$) decreases from 12% to 10% and 3%. For Cu, the corresponding medians are 0.159, 0.307 and 0.217 μm, while $g = 0$ decreases from 28% to 12% and 4%. The distribution tails also contract relative to GO_{10}, with g_{90} changing from 2.164 to 0.706 and 0.880 μm for Ag and from 1.422 to 0.850 and 0.492 μm for Cu. Complete statistics are provided in Table S6.

Collectively, the SEM analysis shows that increasing oxidation and subsequent PEG–NH_2 treatment shift the systems towards smaller particle populations, fewer large agglomerated features and reduced apparent particle contact/overlap, with the strongest changes observed for Cu. Importantly, the non-monotonic median gaps show that this evolution should not be interpreted simply as increased interparticle separation, but as a redistribution of particle sizes and nearest-neighbour configurations. The marked reduction in apparent contact/overlap indicates suppression of the most densely aggregated configurations, which are also the geometries expected to support the strongest short-range electromagnetic coupling [9,10]. Consequently, the morphological evolution may involve a trade-off between extreme junction-driven hotspots and a less heterogeneous particle arrangement. These quantitative trends are further examined at higher spatial resolution by TEM in Section 3.2.2 and provide experimental constraints for the electromagnetic modelling in Section 3.5.

3.2.2. Nanoscale organisation and spatial distribution

TEM analysis (Fig. 7) provides complementary nanoscale evidence of the particle organisation identified by SEM. GO_{10}–Ag exhibits pronounced localised aggregation with extensive particle overlap, whereas GO_{30}–Ag and GO_{30}–PEG–NH_2–Ag show predominantly discrete, individually resolved particles, although some localised clustering remains (Fig. 7a–c). The morphological change is more pronounced for Cu: GO_{10}–Cu contains several large, dense agglomerates, while GO_{30}–Cu and GO_{30}–PEG–NH_2–Cu exhibit substantially fewer large agglomerated regions and a greater prevalence of individually resolved particles (Fig. 7d–f).

These representative TEM observations qualitatively corroborate the quantitative SEM analysis in Section 3.2.1, supporting reduced large-scale agglomeration and altered nanoparticle organisation with increasing oxidation and subsequent PEG–NH_2 treatment, particularly for the Cu-containing systems. TEM is used here for morphological assessment only; no crystallographic information is inferred from these images.

3.3. Thermal decomposition and PEG-Associated loading

TGA/DTGA profiles (Fig. 8) show clear differences with GO oxidation level, PEG–NH_2 treatment and particle incorporation. GO_{30} exhibits substantially greater mass loss below 250 °C than GO_{10}, consistent with its higher oxygen-containing functionality identified by FTIR and XPS. Following PEG–NH_2 treatment, both materials show additional mass loss within the 250–400 °C region and a DTGA feature near 330–340 °C, consistent with a PEG-associated contribution [23–26,40,41].

The additional 250–400 °C mass loss corresponds to apparent PEG-associated loadings of 6.98 wt% for GO_{10}–PEG–NH_2 and 13.09 wt% for GO_{30}–PEG–NH_2, giving an approximately 1.88-fold greater contribution for the more highly oxidised substrate. Sensitivity analysis using varied integration limits and complementary W_{150} normalisation preserved this trend (Section S4 and Table S7). These values are semi-quantitative and do not distinguish covalently attached PEG from non-covalently retained or physically entrapped material. Nevertheless, the greater PEG-associated contribution for GO_{30}–PEG–NH_2 supports a greater extent of PEG-associated interfacial modification, providing experimental context for the subsequent differences in nanoparticle organisation and MD-derived interfacial behaviour.

Ag- and Cu-containing systems also exhibit composition-dependent changes in their decomposition profiles, particularly for GO_{30}-derived materials. However, because the underlying processes cannot be resolved from TGA alone, these profiles are interpreted only as evidence that particle incorporation modifies the thermal decomposition behaviour of the GO-based systems.

3.4. Interfacial interaction Mechanisms and nanocluster Stabilisation

3.4.1. Interaction energetics and interfacial organisation

The calculated interaction-energy descriptor exhibited a systematic dependence on the modelled graphene surface chemistry (Table 1). For Cu_{13}, ΔE changed from − 237.93 kcal•mol^{-1} on PG to − 358.29 kcal•mol^{-1} on GO_{10} and − 462.05 kcal•mol^{-1} on GO_{30}, corresponding to incremental changes ($\Delta\Delta E$) of − 120.36 and − 103.76 kcal•mol^{-1}, respectively. Ag_{13} showed a similar progression, with ΔE changing from − 267.11 kcal•mol^{-1} on PG to − 405.88 kcal•mol^{-1} on GO_{10} and − 485.29 kcal•mol^{-1} on GO_{30}, giving $\Delta\Delta E$ values of − 138.77 and − 79.41 kcal•mol^{-1}. Within the defined hydrated-system interaction-energy framework, the increasingly negative values indicate progressively more favourable nanocluster–substrate interactions with increasing modelled oxidation. Because the atomistic GO_{10} and GO_{30} models represent qualitative low- and high-oxidation analogues rather than compositionally exact representations of the experimental materials, these energetic changes are interpreted as relative oxidation-dependent trends rather than quantitative predictions for the experimental interfaces.

PEG modification produced a further, although smaller, change in the interaction-energy descriptor. ΔE changed from − 462.05

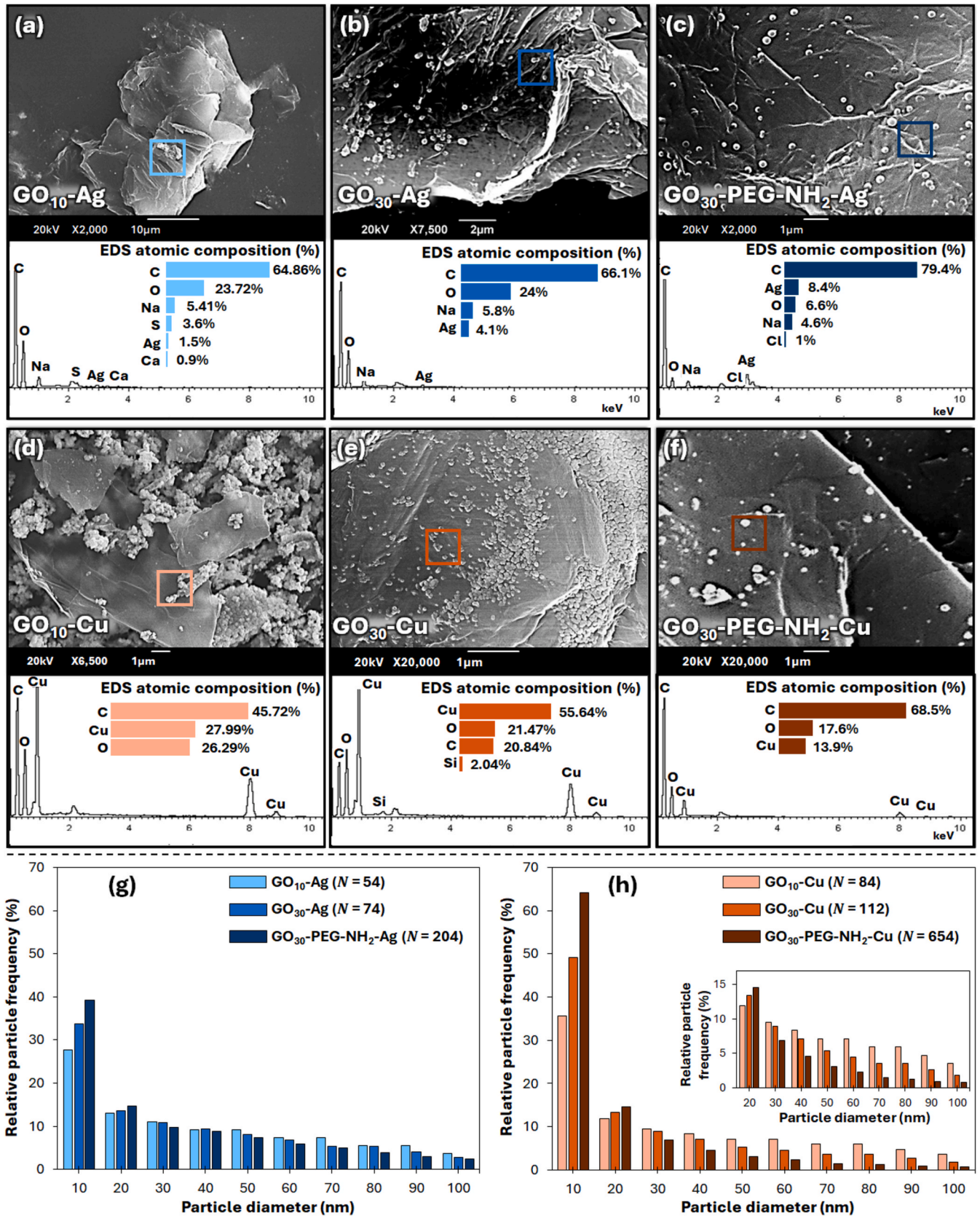


Fig. 6. SEM micrographs, representative local EDS analyses and normalised particle-size distributions of Ag- and Cu-containing nanoparticles supported on GO substrates. (a–c) GO_{10}–Ag, GO_{30}–Ag and GO_{30}–PEG–NH_2–Ag; (d–f) corresponding Cu-containing systems. Coloured boxes indicate the regions analysed by EDS. EDS confirms the elemental presence of Ag and Cu but does not establish their chemical states. (g,h) Normalised particle-size distributions derived from SEM measurements, with the number of analysed particles (*N*) indicated in the legends. The inset in (h) expands the 20–100 nm region.

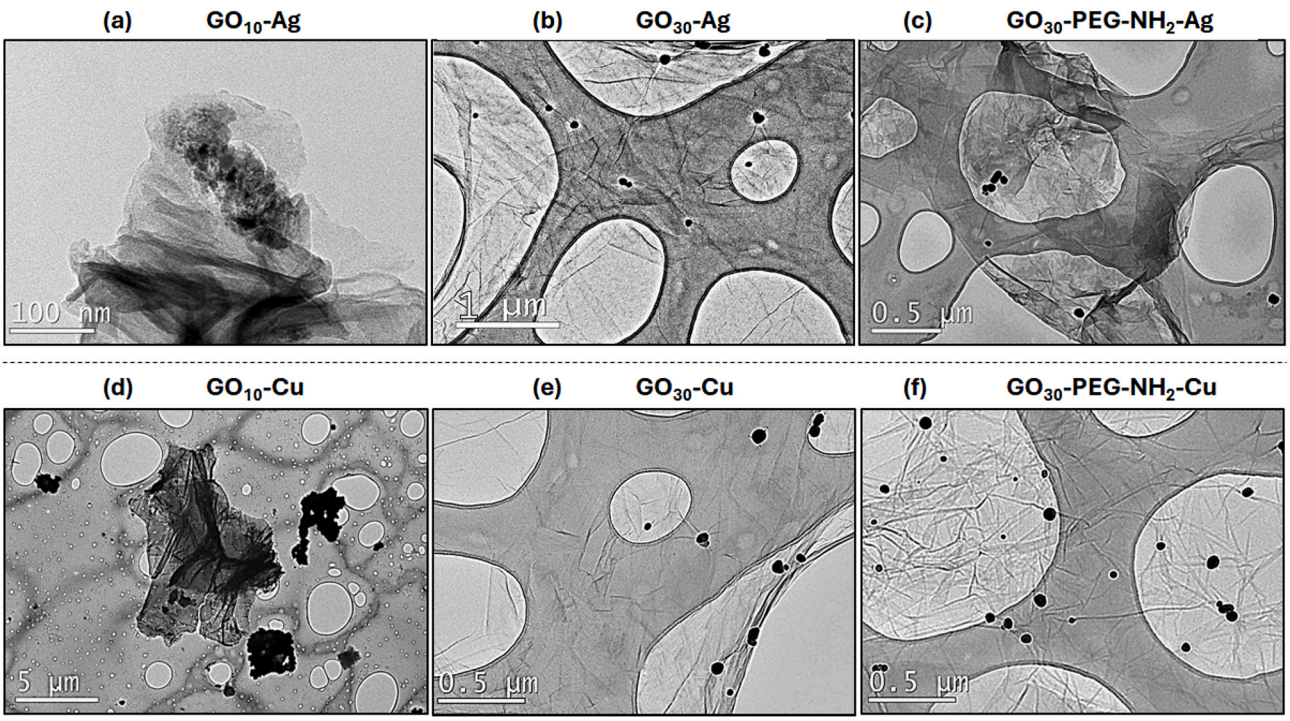


Fig. 7. Representative TEM images showing the nanoscale organisation of Ag- and Cu-containing particles on GO substrates. (a–c) GO_{10}–Ag, GO_{30}–Ag and GO_{30}–PEG–NH_2–Ag; (d–f) GO_{10}–Cu, GO_{30}–Cu and GO_{30}–PEG–NH_2–Cu, respectively. GO_{30} and GO_{30}–PEG–NH_2 show fewer large agglomerated features and a greater prevalence of individually resolved particles than GO_{10}, with the most pronounced differences observed for the Cu-containing systems.

to − 497.91 kcal•mol^{-1} for Cu_{13} and from − 485.29 to − 506.58 kcal•mol^{-1} for Ag_{13} between GO_{30} and GO_{30}–PEG–NH_2, corresponding to $\Delta\Delta E$ values of − 35.86 and − 21.29 kcal•mol^{-1}, respectively. Because the PEG-containing model introduces additional interacting atoms, the GO_{30} and GO_{30}–PEG–NH_2 energies were additionally compared after normalisation by the trajectory-averaged nanocluster–substrate contact area. For Cu_{13}, the contact area decreased from 24.20 Å^2 on GO_{30} to 21.18 Å^2 on GO_{30}–PEG–NH_2, while $\Delta E/A_{contact}$ changed from − 19.10 to − 23.51 kcal•mol^{-1}•Å^{-2}. For Ag_{13}, the corresponding contact areas were 31.93 and 28.15 Å^2, with $\Delta E/A_{contact}$ changing from − 15.20 to − 18.00 kcal•mol^{-1}•Å^{-2}. Thus, the magnitude of the area-normalised interaction-energy descriptor increased by approximately 23% for Cu_{13} and 18% for Ag_{13} following PEG modification. The persistence of this trend after contact-area normalisation indicates that the more negative whole-system interaction energies of the PEG-containing models cannot be attributed solely to differences in interfacial contact area.

The final configurations after 1 ns provide complementary structural context for the interaction-energy analysis (Fig. 9). Both Cu_{13} and Ag_{13} remain associated with the GO_{30} surface, while PEG modification produces a more complex local interfacial environment involving the PEG chains. RDF analysis showed characteristic nanocluster–surface separations of approximately 3.43–3.23 Å for GO_{10}, 3.25–3.27 Å for GO_{30} and 2.83 Å for GO_{30}–PEG–NH_2. Together with the energetic trends, these results support PEG-dependent changes in interfacial organisation within the classical MD model.

Overall, the energetic and structural analyses show that Cu_{13} and Ag_{13} interactions depend on both modelled GO oxidation and PEG modification. Increasing oxidation produces the larger change in the whole-system interaction-energy descriptor, while PEG modification introduces an additional effect that persists after contact-area normalisation, with $\Delta E/A_{contact}$ increasing in magnitude by approximately 23% for Cu_{13} and 18% for Ag_{13}. This indicates that the more favourable interaction is not explained solely by differences in contact area, but reflects a modified local interfacial environment, consistent with the shorter nanocluster–surface separation. These trends support interface-dependent behaviour at the molecular scale but are not interpreted as a direct quantitative explanation of the experimental particle distributions.

3.4.2. *Nanocluster dynamics*

Nanocluster mobility was further evaluated from the MSD trajectories using the anomalous-diffusion relation in Eq. (10), with the fitted Kα and α parameters reported in Table 2. For Cu_{13}, α remained below unity across all surfaces, ranging from 0.403 on GO_{30} to 0.732 on GO_{30}–PEG–NH_2, indicating sublinear MSD scaling over the analysed time window. Ag_{13} showed greater variation, with α = 1.141 on PG and values of 0.506, 0.836 and 0.744 on GO_{10}, GO_{30} and GO_{30}–PEG–NH_2, respectively. Thus, the fitted dynamical response varied across the surface models, although the trends differed between Cu_{13} and Ag_{13}.

The fitted Kα values also varied across the surface models (Table 2), but Kα cannot be interpreted independently of α because its magnitude and units depend on the fitted exponent. The comparatively lower R^2 for GO_{30}–Cu_{13} (0.8861), relative to 0.9381–0.9987 for the other systems, further indicates that the power-law representation describes this trajectory less closely. Accordingly, the fitted parameters are used as comparative descriptors of nanocluster dynamics rather than evidence for a specific diffusion mechanism.

Overall, the MSD analysis shows that nanocluster dynamics are sensitive to the modelled interfacial chemistry, but do not vary monotonically with the interaction-energy trends in Section 3.4.1. This indicates that more favourable nanocluster–surface interactions do not necessarily correspond to proportionally lower lateral mobility, and that energetics and dynamics provide complementary descriptions of the interface. Because only one production trajectory was available for each system, these differences are interpreted as trajectory-specific comparative trends rather than statistically converged mobility differences.

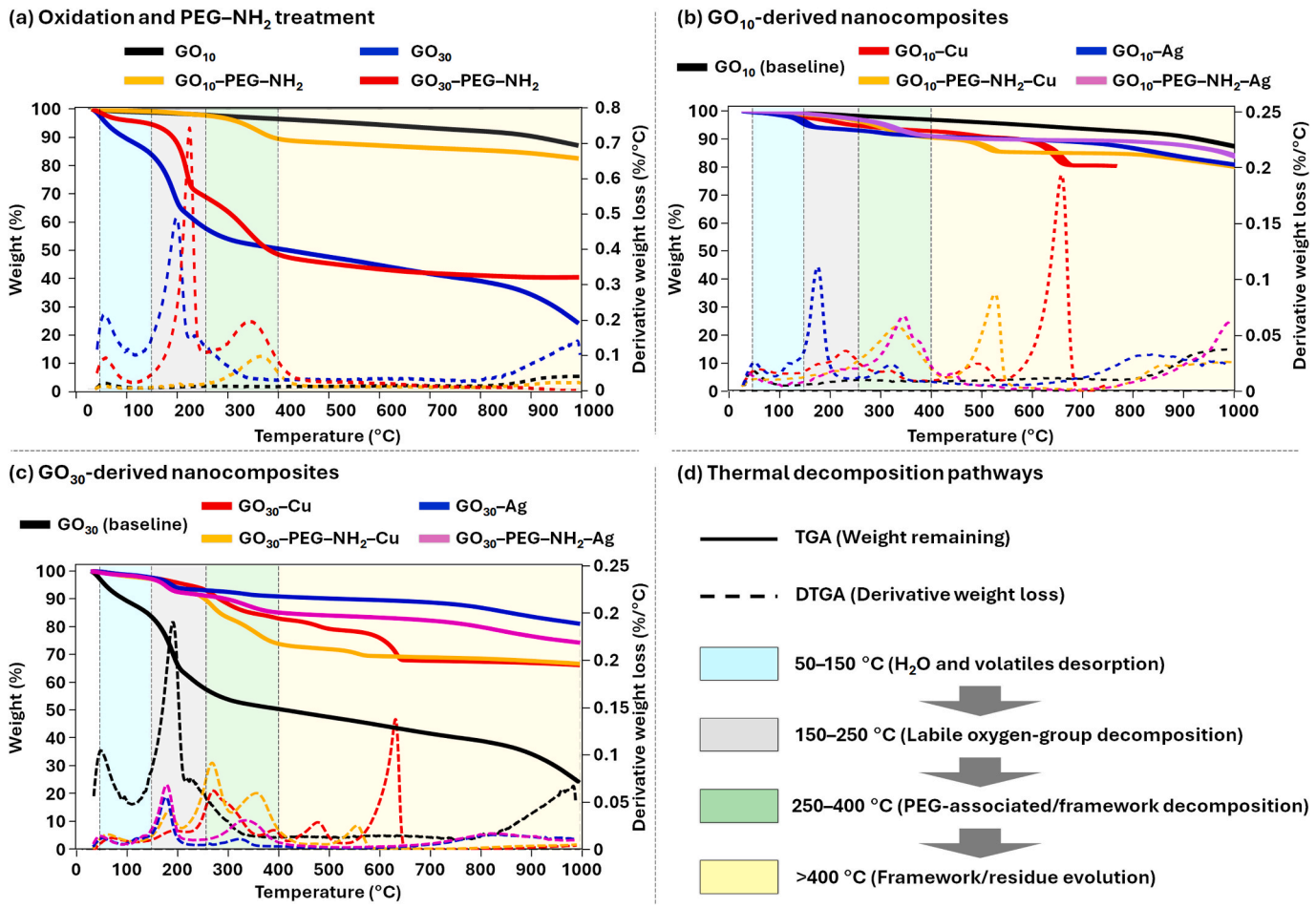


Fig. 8. TGA (solid) and DTGA (dashed) profiles under helium. (a) GO_{10}, GO_{30} and PEG–NH_2-treated counterparts; (b,c) GO_{10}- and GO_{30}-derived Ag- and Cu-containing nanocomposites; and (d) broad thermal decomposition regions. Oxidation level, PEG–NH_2 treatment and particle incorporation produce distinct changes in thermal decomposition behaviour.

Table 1
Interaction-energy descriptors (ΔE), incremental changes ($\Delta\Delta E$), trajectory-averaged nanocluster–substrate contact areas ($A_{contact}$) and area-normalised interaction energies ($\Delta E/A_{contact}$) for Cu_{13} and Ag_{13} across the graphene-based surface models. Contact areas were averaged over the final 300 ps, and normalisation was applied to compare PEG-modified and unmodified GO_{30} interfaces.

Nanocluster	Surface model	ΔE (kcal•mol^{-1})	$\Delta\Delta E$ (kcal•mol^{-1})	$A_{contact}$(Å^2)	$\Delta E/A_{contact}$ (kcal•mol^{-1}•Å^{-2})
Cu_{13}	PG	−237.93	–	–	–
	GO_{10}	−358.29	−120.36	–	–
	GO_{30}	−462.05	−103.76	24.20	−19.10
	GO_{30}–PEG–NH_2	−497.91	−35.86	21.18	−23.51
Ag_{13}	PG	−267.11	–	–	–
	GO_{10}	−405.88	−138.77	–	–
	GO_{30}	−485.29	−79.41	31.93	−15.20
	GO_{30}–PEG–NH_2	−506.58	−21.29	28.15	−18.00

Note: ΔE is the hydrated-system interaction-energy descriptor defined in Eq. (6), and $\Delta\Delta E$ represents the change between successive surface states. More negative values indicate more favourable interactions. $A_{contact}$ is the mean SASA-derived contact area over the final 300 ps, and $\Delta E/A_{contact}$ is the corresponding area-normalised interaction-energy descriptor. Dashes indicate that contact-area normalisation was not applied.

3.5. Optical and plasmonic behaviour of GO–Metal nanostructures

3.5.1. Experimental optical response

UV–Vis spectroscopy was used to assess changes in the optical response of the Ag- and Cu-containing systems following variation in GO oxidation and PEG–NH_2 treatment (Fig. 10). The Ag-containing systems exhibit distinct visible absorption bands, with maxima at approximately 431 nm for isolated Ag nanoparticles, 413 nm for GO_{10}–Ag, 413 nm for GO_{10}–PEG–NH_2–Ag, 411 nm for GO_{30}–Ag and 420 nm for GO_{30}–PEG–NH_2–Ag. These features are consistent with a metallic-like Ag plasmonic contribution [11], although partial surface oxidation cannot be excluded without phase-sensitive characterisation. The changes in band position, intensity and width across the GO-based interfaces are consistent with the accompanying differences in particle size and organisation identified by SEM and TEM.

The Cu-containing systems exhibit substantially broader absorption extending across the visible and near-infrared regions, without a clearly resolved experimental LSPR maximum (Fig. 10b). The measured

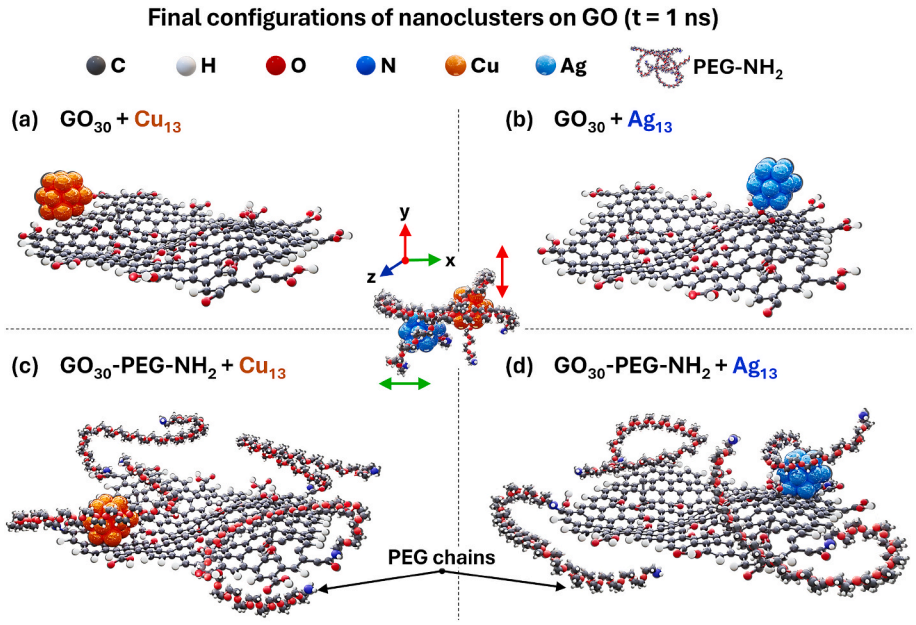


Fig. 9. Final configurations of (a) Cu_{13} and (b) Ag_{13} on GO_{30}, and (c) Cu_{13} and (d) Ag_{13} on GO_{30}–PEG–NH_2 after 1 ns of MD simulation. The configurations illustrate the interfacial organisation of the nanoclusters within the GO_{30} and PEG-modified GO_{30} models. Carbon (C), hydrogen (H), oxygen (O), nitrogen (N), copper (Cu) and silver (Ag) atoms are represented according to the colour scheme shown.

Table 2
Anomalous-diffusion parameters obtained from fitting the nanocluster MSD trajectories to Eq. (10).

Nanocluster	Surface model	K_α (Å^2 • ps$^{-\alpha}$)	α	R^2
Cu_{13}	PG	2.0416 ± 0.0487	0.6859 ± 0.0041	0.9983
	GO_{10}	0.8570 ± 0.0181	0.7067 ± 0.0036	0.9987
	GO_{30}	3.2088 ± 0.3761	0.4027 ± 0.0206	0.8861
	GO_{30}–PEG–NH_2	0.4019 ± 0.0204	0.7316 ± 0.0087	0.9932
Ag_{13}	PG	0.1466 ± 0.0191	1.1409 ± 0.0220	0.9837
	GO_{10}	2.7306 ± 0.2942	0.5057 ± 0.0188	0.9381
	GO_{30}	0.4446 ± 0.0169	0.8363 ± 0.0065	0.9973
	GO_{30}–PEG–NH_2	0.3575 ± 0.0189	0.7441 ± 0.0091	0.9931

Note: K_α and α were obtained by fitting $MSD(t) = K_\alpha t^\alpha$ over 0–495 ps. Reported uncertainties are fitting standard errors and do not represent variability between independent trajectories. R^2 was calculated on the linear MSD scale.

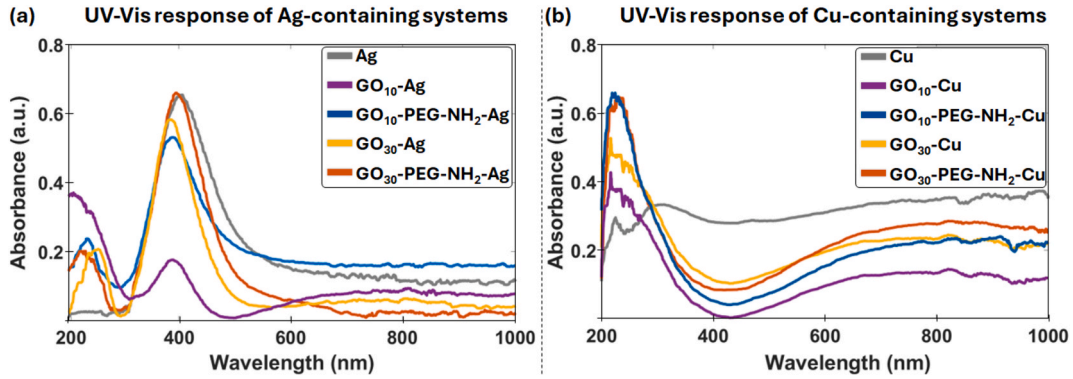


Fig. 10. UV–Vis absorption spectra of (a) Ag-containing and (b) Cu-containing systems supported on GO_{10} and GO_{30} before and after PEG–NH_2 treatment. The Ag-containing systems exhibit distinct visible absorption bands, whereas the Cu-containing systems show broader visible–near-infrared responses without a clearly resolved LSPR maximum.

response therefore cannot be assigned unambiguously to metallic Cu. Oxidation can substantially modify the Cu plasmonic response [12,13], while aggregation, polydispersity, scattering and absorption from the GO-based substrate may further broaden the measured spectrum [6,42]. Nevertheless, the spectra vary systematically across the GO and PEG–NH_2-treated interfaces. These experimental optical differences provide the basis for the controlled FDTD analysis of particle-size and interparticle-separation effects in Sections 3.5.2 and 3.5.3, followed by

the experiment-informed assemblies in Section 3.5.4.

3.5.2. Particle-Size-Dependent optical response

The experimentally measured particle-size distributions provide the basis for the controlled 10–100 nm FDTD size sweep (Fig. 11a,b). For Ag-containing systems, D_{50} decreases from 28.3 nm for GO_{10}–Ag to 22.5 nm for GO_{30}–Ag and 17.3 nm for GO_{30}–PEG–NH_2–Ag, while D_{90} decreases from 78.7 to 74.0 and 68.6 nm, respectively. The corresponding Cu distributions shift more strongly towards smaller particles, with D_{50} decreasing from 22.5 to 10.7 and 7.8 nm and D_{90} from 77.2 to 64.5 and 39.5 nm. Thus, the simulated diameter range captures the principal experimental size regime, although the D_{50} of GO_{30}–PEG–NH_2–Cu lies slightly below the 10 nm lower bound. The spherical models are therefore used to isolate diameter-dependent optical effects rather than to reproduce the complete experimental size and shape distributions.

Increasing particle diameter produced pronounced changes in both the calculated spectral and near-field responses (Fig. 11c–f). For Ag, λ_{LSPR} shifts from approximately 396 to 492.5 nm between 10 and 100 nm, corresponding to a 96.25 nm redshift, while the idealised Cu model shifts from approximately 536.25 to 597.5 nm, a 61.25 nm redshift. These trends are consistent with established size-dependent electrodynamic behaviour [6,13]. However, the near-field response does not follow the same monotonic size dependence. For Ag, the maximum $|E/E_0|$ reaches approximately 15.3 at 50 nm before decreasing at larger diameters, whereas the Cu response increases across the simulated range to approximately 8.33 at 100 nm. Using the fourth-power approximation in Eq. (14), these peak field amplitudes correspond to predicted electromagnetic enhancement estimates, EF_{EM}, of approximately 5.5×10^4 for Ag and 4.8×10^3 for Cu, respectively. Thus, particle sizes that produce the greatest spectral redshift do not necessarily generate the strongest local fields, and the relationship is metal dependent. Particle-size redistribution can therefore alter far-field resonance and near-field enhancement differently, making the preferred size regime dependent on the targeted optical function. The Ag and Cu simulations represent an idealised metallic reference and are not used to establish the chemical state of the corresponding experimental metal-containing particles.

3.5.3. Interparticle-Separation-Dependent coupling

The experimentally measured nearest-neighbour distributions show that interparticle organisation changes substantially across the GO-based interfaces (Fig. 12a,b). For Ag-containing systems, the median apparent surface gap changes from 0.661 μm for GO_{10}–Ag to 0.230 μm for GO_{30}–Ag and 0.424 μm for GO_{30}–PEG–NH_2–Ag, while the apparent contact/overlap fraction ($g = 0$) decreases from 12% to 10% and 3%, respectively. For Cu, the corresponding median gaps are 0.159, 0.307 and 0.217 μm, with $g = 0$ decreasing from 28% to 12% and 4%. The

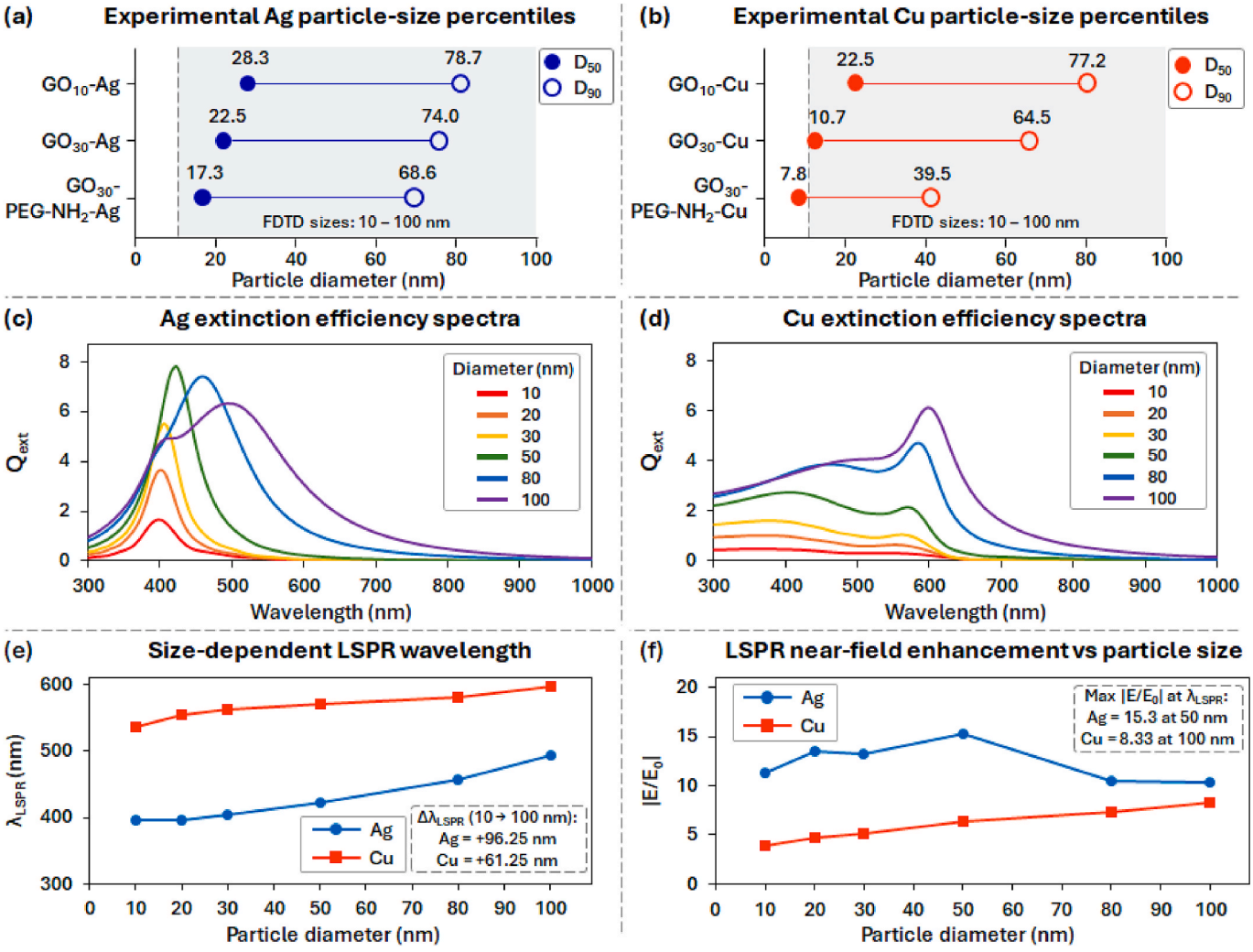


Fig. 11. Experimental particle-size distributions and size-dependent FDTD response of Ag and Cu nanoparticles. (a,b) Experimental D_{50} and D_{90} diameters relative to the 10–100 nm FDTD size range. (c,d) Calculated extinction-efficiency spectra, Q_{ext}, for spherical Ag and Cu nanoparticles with diameters of 10–100 nm. (e) Size-dependent LSPR wavelength, λ_{LSPR}, and (f) maximum near-field amplitude, $|E/E_0|$, evaluated at the corresponding LSPR wavelength.

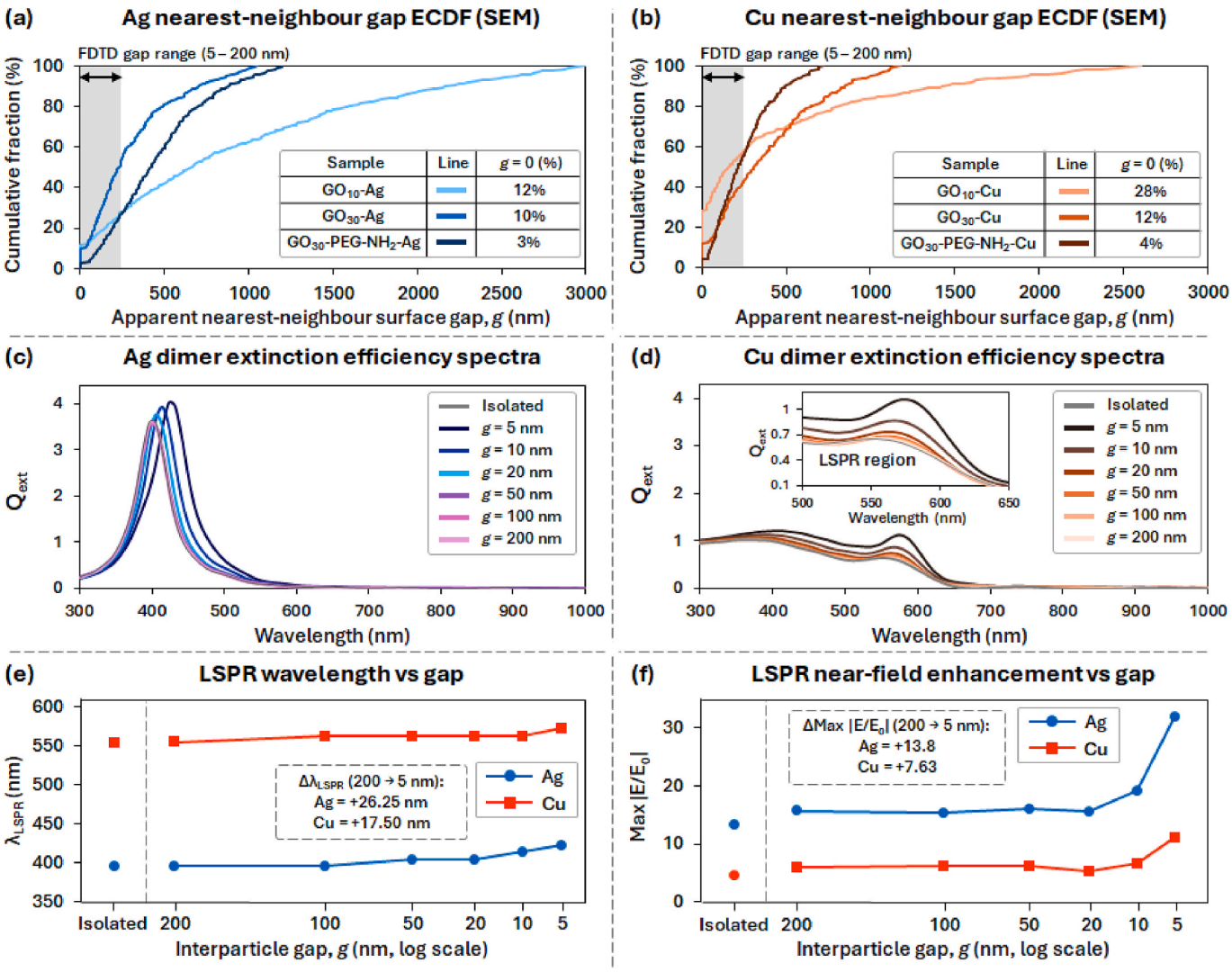


Fig. 12. Experimental nearest-neighbour spacing distributions and separation-dependent FDTD response of Ag and Cu nanoparticles. (a,b) ECDFs of apparent nearest-neighbour surface gaps for the Ag- and Cu-containing systems, with the 5–200 nm FDTD gap range indicated and apparent contact/overlap fractions ($g = 0$) reported separately. (c,d) Calculated extinction-efficiency spectra, Q_{ext}, for 20 nm Ag and Cu dimers with metal–metal gaps of 5–200 nm. (e) Gap-dependent LSPR wavelength, λ_{LSPR}, and (f) maximum near-field amplitude, $|E/E_0|$, evaluated at the corresponding LSPR wavelength.

controlled FDTD sweep of 5–200 nm therefore probes the short-separation regime of these experimental distributions rather than reproducing their full spacing range.

Using 20 nm spherical dimers, decreasing the metal–metal gap from 200 to 5 nm progressively strengthens electromagnetic coupling and red-shifts the calculated resonance (Fig. 12c–f), consistent with established plasmon-hybridisation behaviour [9,10]. The Ag model shows an approximately 26.25 nm increase in λ_{LSPR} and a 13.8 increase in maximum $|E/E_0|$, while the corresponding Cu changes are approximately 17.50 nm and 7.63. However, if such close junctions arise from aggregation, the resulting hotspots may be highly localised and geometry-sensitive. Thus, stronger local-field enhancement can come at the expense of a more heterogeneous optical response. The dimer calculations therefore provide a reference for interpreting the short-gap portion of the experimental spacing distributions.

3.5.4. *Experiment-Informed assemblies and electromagnetic enhancement*

Experiment-informed FDTD assemblies were constructed to examine how the experimentally observed changes in particle size and spatial organisation affect the optical response (Fig. 13; Table S10). The calculated λ_{LSPR} shifts from 475 to 440 and 422.5 nm across GO_{10}–Ag, GO_{30}–Ag and GO_{30}–PEG–NH_2–Ag, respectively, while the corresponding Cu models shift from 597.5 to 580 and 571.25 nm (Fig. 13a–h). At the respective resonances, the near-field maps show strongly non-uniform local enhancement close to the nanoparticle plane, with the field magnitude decreasing with increasing distance from the interface.

The optical response also becomes progressively sharper across the model series. Q_{res} increases from 2.35 to 2.69 and 3.34 for the Ag assemblies and from 9.51 to 15.94 and 22.71 for the Cu assemblies (Fig. 13i). In parallel, the absorption contribution to extinction increases from 37.2% to 48.1% and 59.0% for Ag and from 56.7% to 83.5% and 97.3% for Cu (Fig. 13j). Despite this increase in resonance quality, the peak sampled-plane $|E/E_0|$ decreases as the minimum metal–metal separation increases across the experiment-informed assemblies (Fig. 13k,l), consistent with the controlled dimer results in Section 3.5.3. The corresponding peak EF_{EM} estimates decrease by approximately sevenfold across the Ag model series and fiftyfold across the Cu series from GO_{10} to GO_{30}–PEG–NH_2, corresponding to a substantially larger relative decrease in the Cu assemblies. Exact EF_{EM} values are provided in Table S10. These values represent local peak electromagnetic estimates rather than spatially averaged or experimentally measured SERS enhancement factors. Because particle size, number and spatial arrangement vary simultaneously in these assemblies, the minimum gap

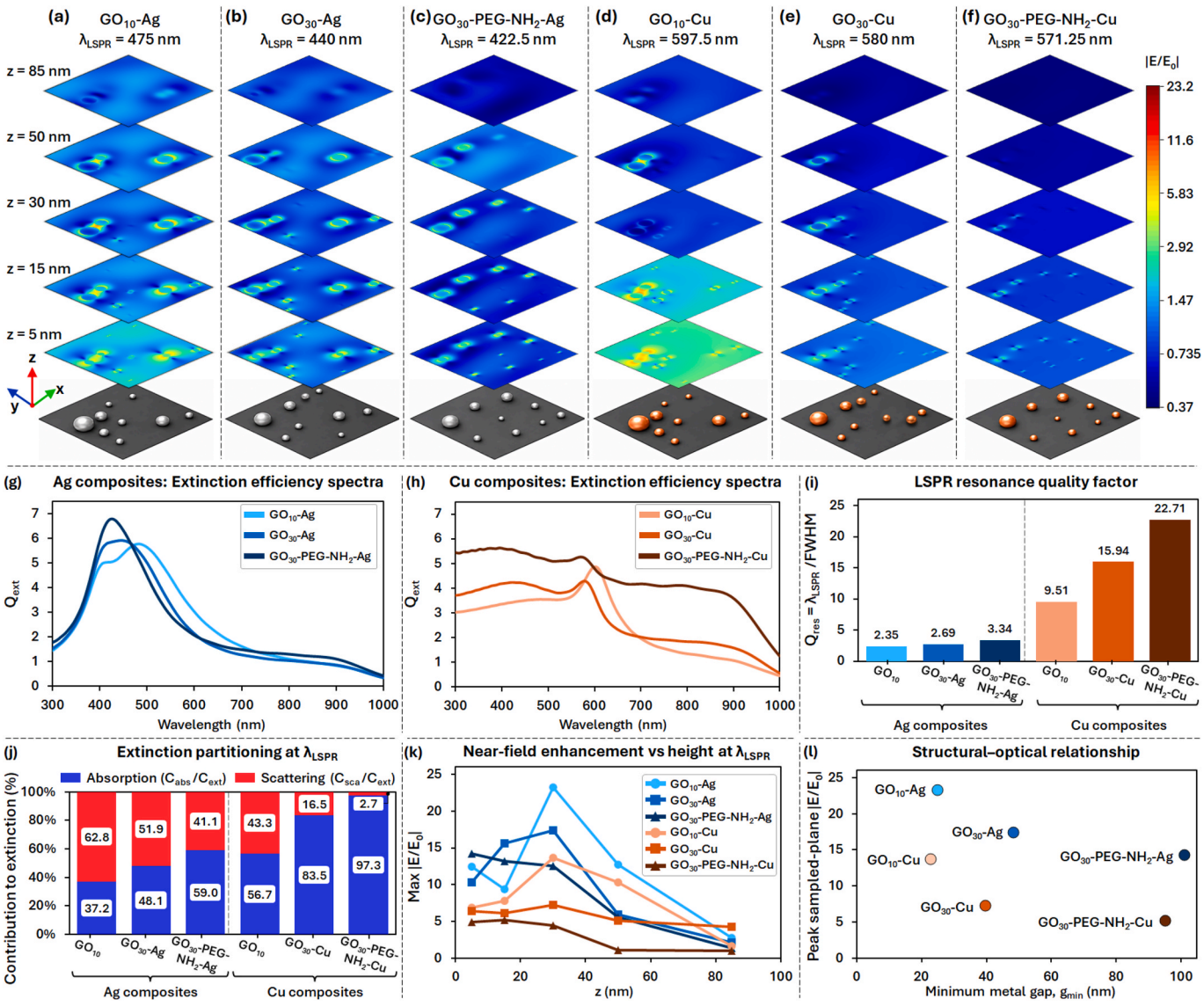


Fig. 13. Experiment-informed FDTD analysis of Ag- and Cu-containing GO assemblies. (a–f) Near-field distributions, $|E/E_0|$, at the calculated λ_{LSPR} for GO_{10}, GO_{30} and GO_{30}–PEG–NH_2 assemblies, sampled at increasing heights above the nanoparticle plane. (g,h) Extinction-efficiency spectra for the Ag and Cu assemblies. (i) LSPR resonance quality factor, Q_{res}. (j) Absorption and scattering contributions to extinction at λ_{LSPR}. (k) Maximum near-field amplitude as a function of sampling height. (l) Relationship between minimum metal–metal gap and peak sampled-plane $|E/E_0|$.

is interpreted as one contributing structural parameter rather than the sole determinant of the near-field response.

Overall, the experiment-informed models reveal a trade-off between extreme hotspot intensity and a more controlled optical response. Increasing GO oxidation and PEG–NH_2 treatment are associated experimentally with smaller, less-contacting particle populations, while the corresponding models exhibit higher Q_{res} and more absorption-dominated extinction but lower peak $|E/E_0|$. This indicates that reducing close-contact geometries can suppress extreme junction-driven hotspots while promoting sharper, more spectrally defined plasmonic behaviour. The Ag and Cu calculations represent idealised metallic reference models and do not establish the chemical state of the experimental particles; the calculated field enhancement is therefore interpreted as a predicted electromagnetic response rather than experimental SERS performance [35].

4. Conclusion

This study establishes a multiscale relationship between GO surface chemistry, PEG-associated modification, nanoparticle organisation and optical response in Ag- and Cu-containing nanocomposites. Higher surface oxygen content and subsequent PEG–NH_2 treatment were associated with greater apparent PEG-associated loading, smaller particle populations, fewer large agglomerated features and reduced apparent particle contact/overlap, particularly for Cu-containing systems. The non-monotonic nearest-neighbour spacing shows that this evolution reflects redistribution of particle organisation rather than a simple increase in separation.

MD simulations provided complementary atomistic evidence of interface-dependent behaviour. Increasing modelled oxidation produced more favourable hydrated interaction-energy descriptors, while PEG modification produced an additional effect that persisted after contact-area normalisation, with $\Delta E/A_{contact}$ increasing in magnitude by approximately 23% for Cu_{13} and 18% for Ag_{13}. These results are interpreted comparatively because of the scale and compositional differences between the atomistic and experimental systems.

FDTD modelling showed that particle size and separation govern spectral position and local-field enhancement differently. Experiment-

informed assemblies exhibited higher resonance quality and more absorption-dominated extinction with increasing oxidation and PEG–NH_2 treatment, while extreme hotspot intensity decreased as close particle contacts were reduced. This reflects a trade-off in which reduced agglomeration limits highly localised, junction-dominated enhancement and decreases the dependence of the electromagnetic response on a small number of extreme contact geometries, while promoting a sharper and more spectrally defined plasmonic response. Overall, GO surface chemistry and PEG-associated modification provide relevant design parameters for tuning nanoparticle organisation and plasmonic behaviour. The calculated enhancement represents a predicted electromagnetic response rather than experimentally demonstrated SERS performance.

CRediT authorship contribution statement

Patrick Irigo: Writing – review & editing, Writing – original draft, Visualization, Validation, Software, Methodology, Investigation, Formal analysis, Data curation, Conceptualization. **Miriam Roldán-Matilla:** Writing – review & editing, Validation, Methodology, Formal analysis. **María Fuencisla Gilsanz:** Investigation, Data curation. **Javier Perez-Pineiro:** Investigation. **Arisbel Cerpa-Naranjo:** Writing – review & editing, Resources. **Ian Johnston:** Resources, Software, Writing – review & editing, Funding acquisition. **Isabel Lado-Touriño:** Writing – review & editing, Validation, Software. **Guogang Ren:** Conceptualization, Funding acquisition, Methodology, Resources, Validation, Writing – review & editing.

Declaration of competing interest

The authors declare that they have no known competing financial interests or personal relationships that could have appeared to influence the work reported in this paper.

Appendix A. Supplementary data

Supplementary data to this article can be found online at https://doi.org/10.1016/j.apsusc.2026.168817. The Supporting Information is available free of charge and includes FTIR peak assignments (Table S1); XPS survey composition and survey spectra (Table S2 and Fig. S1); high-resolution C 1 s and O 1 s fitting parameters (Table S3 and S4); supplementary N 1 s analysis (Fig. S2); quantitative particle-size and nearest-neighbour spacing statistics (Table S5 and S6); TGA-based apparent PEG-associated loading and sensitivity analysis (Table S7); FDTD mesh-convergence analysis (Fig. S3 and Table S8); PEG-shell thickness sensitivity analysis (Fig. S4 and Table S9); and structural, optical and coordinate data for the experiment-informed FDTD assemblies (Table S10-S12).

Data availability

Data will be made available on request.

References

[1] J. Wu, H. Lin, D. J. Moss, K. P. Loh, and B. Jia, "Graphene oxide for photonics, electronics and optoelectronics," *Nature Reviews Chemistry 2023 7:3*, vol. 7, no. 3, pp. 162–183, Jan. 2023, doi: 10.1038/s41570-022-00458-7.

[2] S. Ganguly, J. Sengupta, C.M. Hussain, Surface and interface functionalization of graphene and beyond: strategies for targeted applications, Nanoscale 18 (16) (Apr. 2026) 8422–8441, https://doi.org/10.1039/D6NR00009F.

[3] M. Mahdavi, A. Fattahi, E. Tajkhorshid, S. Nouranian, Molecular Insights into the Loading and Dynamics of Doxorubicin on PEGylated Graphene Oxide Nanocarriers, ACS Appl. Bio Mater. 3 (3) (Mar. 2020) 1354–1363, https://doi.org/10.1021/ACSABM.9B00956.

[4] M. Roldán-Matilla, P. Irigo, M.L. Rojas-Cervantes, M.P. Arce, J. Pérez-Piñeiro, M. F. Gilsanz, I. Lado-Touriño, A. Cerpa-Naranjo, G. Ren, Structural characterisation and dynamic modelling of pegylated graphene oxide with Ag and Cu nanocluster, Appl. Surf. Sci. 688 (Apr. 2025) 162430, https://doi.org/10.1016/J.APSUSC.2025.162430.

[5] R.K. Layek, A.K. Nandi, A review on synthesis and properties of polymer functionalized graphene, Polymer (guildf) 54 (19) (Aug. 2013) 5087–5103, https://doi.org/10.1016/J.POLYMER.2013.06.027.

[6] K.L. Kelly, E. Coronado, L.L. Zhao, G.C. Schatz, The Optical Properties of Metal Nanoparticles: the Influence of size, Shape, and Dielectric Environment, J. Phys. Chem. B 107 (3) (Jan. 2003) 668–677, https://doi.org/10.1021/JP026731Y.

[7] F. Tian, F. Bonnier, A. Casey, A.E. Shanahan, H.J. Byrne, Surface enhanced Raman scattering with gold nanoparticles: effect of particle shape, Anal. Methods 6 (22) (Oct. 2014) 9116–9123, https://doi.org/10.1039/C4AY02112F.

[8] M. Kasztelan, S. Zoladek, W. Wieczorek, B. Palys, Template-Free Synthesized Gold Nanobowls Composed with Graphene Oxide for Ultrasensitive SERS Platforms, J. Phys. Chem. C 127 (34) (Aug. 2023) 16960–16969, https://doi.org/10.1021/ACS.JPCC.3C03607.

[9] P.K. Jain, W. Huang, M.A. El-Sayed, On the Universal Scaling Behavior of the Distance Decay of Plasmon Coupling in Metal Nanoparticle Pairs: a Plasmon Ruler Equation, Nano Lett. 7 (7) (Jul. 2007) 2080–2088, https://doi.org/10.1021/NL071008A.

[10] P. Nordlander, C. Oubre, E. Prodan, K. Li, M.I. Stockman, Plasmon Hybridization in Nanoparticle Dimers, Nano Lett. 4 (5) (May 2004) 899–903, https://doi.org/10.1021/NL049681C.

[11] K. Yuan, L. Chen, Y. Chen, Optical Engineering of Uniformly decorated Graphene Oxide Nanoflakes via in Situ growth of Silver Nanoparticles with Enhanced Plasmonic Resonance, ACS Appl. Mater. Interfaces 6 (23) (Dec. 2014) 21069–21077, https://doi.org/10.1021/AM505916Q.

[12] F. Gonzalez-Posada, R. Sellappan, B. Vanpoucke, D. Chakarov, Oxidation of copper nanoparticles in water monitored in situ by localized surface plasmon resonance spectroscopy, RSC Adv. 4 (40) (May 2014) 20659–20664, https://doi.org/10.1039/C3RA47473A.

[13] O.A. Yeshchenko, I.M. Dmitruk, A.M. Dmytruk, A.A. Alexeenko, Influence of annealing conditions on size and optical properties of copper nanoparticles embedded in silica matrix, Mater. Sci. Eng. B 137 (1–3) (Feb. 2007) 247–254, https://doi.org/10.1016/J.MSEB.2006.11.030.

[14] J.P. Camden, J.A. Dieringer, Y. Wang, D.J. Masiello, L.D. Marks, G.C. Schatz, R. P. Van Duyne, Probing the Structure of Single-Molecule Surface-Enhanced Raman Scattering Hot spots, J. Am. Chem. Soc. 130 (38) (Sep. 2008) 12616–12617, https://doi.org/10.1021/JA8051427.

[15] A. Liu, C. Gao, J. Xue, Y. Xie, X. Miao, T. Chen, A. Wu, J. Lin, Toward reproducible SERS biosensing: analysing instability origins and mitigation approaches from sample preparation to detection, J. Mater. Chem. B 14 (10) (Mar. 2026) 3071–3092, https://doi.org/10.1039/D5TB02751A.

[16] P. Dey, Aiming for Maximized and Reproducible Enhancements in the Obstacle race of SERS, ACS Measurement Science Au 3 (6) (Dec. 2023) 434–443, https://doi.org/10.1021/ACSMEASURESCIAU.3C00037.

[17] X. Yu, H. Cai, W. Zhang, X. Li, N. Pan, Y. Luo, X. Wang, J.G. Hou, Tuning Chemical Enhancement of SERS by Controlling the Chemical Reduction of Graphene Oxide Nanosheets, ACS Nano 5 (2) (Feb. 2011) 952–958, https://doi.org/10.1021/NN102291J.

[18] M. Roldán-Matilla, A. Cerpa-Naranjo, and I. Lado-Touriño, "Exploring Metal Cluster Interactions with Functionalized Graphene via Molecular Dynamics Simulation," *C 2024, Vol. 10, Page 107*, vol. 10, no. 4, p. 107, Dec. 2024, doi: 10.3390/C10040107.

[19] I. Lado-Touriño, A. Páez-Pavón, Interaction between graphene-based materials and small ag, cu, and cuo clusters: a molecular dynamics study, Nanomaterials 11 (6) (Jun. 2021) 1378, https://doi.org/10.3390/NANO11061378.

[20] D. Chaparro, E. Goudeli, Design of engineered nanoparticles for biomedical applications by computational modeling, Nanoscale 17 (16) (Apr. 2025) 9705–9737, https://doi.org/10.1039/D4NR05199H.

[21] W.Z. Liang, J. Huang, J. Sun, P. Zhang, A. Li, Multiscale modeling and simulation of surface-enhanced spectroscopy and plasmonic photocatalysis, Wiley Interdiscip. Rev.: Comput. Mol. Sci. 13 (5) (Sep. 2023) e1665.

[22] M. Gakiya-Teruya, L. Palomino-Marcelo, and J. C. F. Rodriguez-Reyes, "Synthesis of Highly Concentrated Suspensions of Silver Nanoparticles by Two Versions of the Chemical Reduction Method," *Methods and Protocols 2019, Vol. 2, Page 3*, vol. 2, no. 1, p. 3, Dec. 2018, doi: 10.3390/MPS2010003.

[23] K. Rahme, L. Chen, R.G. Hobbs, M.A. Morris, C. O'Driscoll, J.D. Holmes, PEGylated gold nanoparticles: polymer quantification as a function of PEG lengths and nanoparticle dimensions, RSC Adv. 3 (17) (Apr. 2013) 6085–6094, https://doi.org/10.1039/C3RA22739A.

[24] I.A. Vacchi, C. Spinato, J. Raya, A. Bianco, C. Ménard-Moyon, Chemical reactivity of graphene oxide towards amines elucidated by solid-state NMR, Nanoscale 8 (28) (Jul. 2016) 13714–13721, https://doi.org/10.1039/C6NR03846H.

[25] I.R.S. Menezes, N.R.S. Araújo, B.C.R. Araújo, T. Sakai, R.M. Lago, R.C.O. Sebastião, Shedding light on the mechanism of graphene oxide thermal decomposition: a kinetic study using isoconversional method and artificial neural network, Thermochim Acta 721 (Mar. 2023) 179454, https://doi.org/10.1016/J.TCA.2023.179454.

[26] S. Karimi, I. Ghasemi, F. Abbassi-Sourki, M. Samara, N.R. Demarquette, PEG-Grafted Graphene/PLLA Nanocomposites: effect of PEG Chain Length on Crystallization Kinetics of PLLA, ACS Omega 7 (35) (Sep. 2022) 31197–31204, https://doi.org/10.1021/ACSOMEGA.2C03397.

[27] S. Nosé, A molecular dynamics method for simulations in the canonical ensemble, Mol. Phys. 52 (2) (1984) 255–268, https://doi.org/10.1080/00268978400101201.

[28] W. G. Hoover, "Canonical dynamics: Equilibrium phase-space distributions," *Phys. Rev. A (Coll. Park).*, vol. 31, no. 3, p. 1695, Mar. 1985, doi: 10.1103/PhysRevA.31.1695.
[29] H. Sun, Compass: an ab initio force-field optimized for condensed-phase applications - Overview with details on alkane and benzene compounds, J. Phys. Chem. B 102 (38) (Sep. 1998) 7338–7364, https://doi.org/10.1021/JP980939V.
[30] K.S. Yee, Numerical solution of initial Boundary Value Problems Involving Maxwell's Equations in Isotropic Media, IEEE Trans. Antennas Propag. 14 (3) (1966) 302–307, https://doi.org/10.1109/TAP.1966.1138693.
[31] H. J. Hagemann, W. Gudat, and C. Kunz, "Optical constants from the far infrared to the x-ray region: Mg, Al, Cu, Ag, Au, Bi, C, and Al_2O_3," *JOSA, Vol. 65, Issue 6, pp. 742-744*, vol. 65, no. 6, pp. 742–744, Jun. 1975, doi: 10.1364/JOSA.65.000742.
[32] G.G. Politano, C. Versace, C. Vena, M. Castriota, F. Ciuchi, A. Fasanella, G. Desiderio, E. Cazzanelli, Physical investigation of electrophoretically deposited graphene oxide and reduced graphene oxide thin films, J. Appl. Phys. 120 (19) (2016) Nov, https://doi.org/10.1063/1.4968000.
[33] D. Shah, T. Roychowdhury, J. N. Hilfiker, and M. R. Linford, "Polyethylene glycol: Optical constants from 191 to 1688 nm (0.735–6.491 eV) by spectroscopic ellipsometry," *Surface Science Spectra*, vol. 27, no. 1, Jun. 2020, doi: 10.1116/1.5095949.
[34] F. Shao, Z. Lu, C. Liu, H. Han, K. Chen, W. Li, Q. He, H. Peng, J. Chen, Hierarchical nanogaps within bioscaffold arrays as a high-performance SERS substrate for animal virus biosensing, ACS Appl. Mater. Interfaces 6 (9) (May 2014) 6281–6289, https://doi.org/10.1021/AM4045212.
[35] E.C. Le Ru, E. Blackie, M. Meyer, P.G. Etchegoint, Surface Enhanced Raman Scattering Enhancement Factors: a Comprehensive Study, J. Phys. Chem. C 111 (37) (Sep. 2007) 13794–13803, https://doi.org/10.1021/JP0687908.
[36] A.M. Dimiev, C.E. Halbig, A. Talyzin, A critical Review to Avoid Common Misinterpretations in Characterizing Graphene Oxide, Chem. Rev. 126 (5) (Mar. 2026) 3055–3088, https://doi.org/10.1021/ACS.CHEMREV.5C00756.
[37] J. Charmi, H. Nosrati, J. Mostafavi Amjad, R. Mohammadkhani, and H. Danafar, "Polyethylene glycol (PEG) decorated graphene oxide nanosheets for controlled release curcumin delivery," *Heliyon*, vol. 5, no. 4, p. e01466, Apr. 2019, doi: 10.1016/J.HELIYON.2019.E01466.
[38] H.J. Shin, K.K. Kim, A. Benayad, S.M. Yoon, H.K. Park, I.S. Jung, M.H. Jin, H. K. Jeong, J.M. Kim, J.Y. Choi, et al., Efficient reduction of graphite oxide by sodium borohydride and its effect on electrical conductance, Adv. Funct. Mater. 19 (12) (Jun. 2009) 1987–1992, https://doi.org/10.1002/ADFM.200900167.
[39] R. Zhao, M. Lv, Y. Li, M. Sun, W. Kong, L. Wang, S. Song, C. Fan, L. Jia, S. Qiu, et al., Stable Nanocomposite based on PEGylated and Silver Nanoparticles Loaded Graphene Oxide for Long-Term Antibacterial activity, ACS Appl. Mater. Interfaces 9 (18) (May 2017) 15328–15341, https://doi.org/10.1021/ACSAMI.7B03987.
[40] J. Manson, D. Kumar, B. J. Meenan, and D. Dixon, "Polyethylene glycol functionalized gold nanoparticles: the influence of capping density on stability in various media," *Gold Bulletin 2011 44:2*, vol. 44, no. 2, pp. 99–105, Apr. 2011, doi: 10.1007/S13404-011-0015-8.
[41] Z. Sanei, T. Ghanbari, and A. Sharif, "Polyethylene glycol-grafted graphene oxide nanosheets in tailoring the structure and reverse osmosis performance of thin film composite membrane," *Scientific Reports 2023 13:1*, vol. 13, no. 1, pp. 16940-, Oct. 2023, doi: 10.1038/s41598-023-44129-z.
[42] Q. Lai, S. Zhu, X. Luo, M. Zou, S. Huang, Ultraviolet-visible spectroscopy of graphene oxides, AIP Adv. 2 (3) (Sep. 2012) 32146, https://doi.org/10.1063/1.4747817.